Insights into the long-term (2005-2021) spatiotemporal evolution of summer ozone production sensitivity in the Northern Hemisphere derived with OMI

Matthew S. Johnson[1*], Sajeev Philip[2], Scott Meech[3], Rajesh Kumar[3], Meytar Sorek-Hamer[4], Yoichi P. Shiga[4], Jia Jung[1,5]

[1]Earth Science Division, NASA Ames Research Center, Moffett Field, CA 94035, USA
[2]Centre for Atmospheric Sciences, Indian Institute of Technology Delhi, New Delhi, India
[3]Research Applications Laboratory, NSF National Center for Atmospheric Research, Boulder, CO 80305, USA
[4]NASA Academic Mission Services by Universities Space Research Association at NASA Ames Research Center, Mountain View, CA, USA
[5]Bay Area Environmental Research Institute, Moffett Field, CA 94035, USA

*Correspondence: Matthew S. Johnson (matthew.s.johnson@nasa.gov)

Abstract. Tropospheric ozone (O_3) formation depends on the relative abundance of precursor species, nitrogen oxides (NO_x) and volatile organic compounds (VOCs). Advancements in satellite retrievals of formaldehyde (HCHO) and nitrogen dioxide (NO_2) vertical column densities (VCDs), and the corresponding $HCHO/NO_2$ ratios (FNRs), provide the opportunity to diagnose the spatiotemporal evolution of O_3 production sensitivity regimes. This study investigates trends of summertime VCD HCHO, NO_2, and Ozone Monitoring Instrument (OMI)-derived FNRs in the Northern Hemisphere from 2005 to 2021. FNR trends were analysed for polluted regions, specifically for 46 highly populated cities, over the entire 17-year period and in 2020 when global anthropogenic emissions were reduced due to COVID-19 lockdown restrictions. It was determined that OMI-derived FNRs have increased on average ~65% across cities in the Northern Hemisphere. Increasing OMI-derived FNRs indicates a general transition from radical-limited to NO_x-limited regimes. The increasing trend is driven by reduced NO_2 concentrations because of emission control strategies of NO_x. OMI FNR trends were compared to ground-based in situ measurements in US cities and determined they can capture the trends in increasing FNRs (R = 0.91) and decreasing NO_2 (R = 0.98) occurring at the surface. OMI FNRs in urban areas were higher (~20%) in 2020 for most cities studied here compared to 2019 and 2021. In addition to studying the longest period of OMI FNRs across the Northern Hemisphere to-date, the capabilities and challenges of using satellite VCD FNRs to study surface-level O_3 production sensitivity regimes are discussed.

Short Summary. Satellites, such as the Ozone Monitoring Instrument (OMI), retrieve proxy species of ozone (O_3) formation (formaldehyde and nitrogen dioxide) and the ratios (FNRs) which can define O_3 production sensitivity regimes. Here we investigate trends of OMI FNRs from 2005 to 2021 and they have increased in major cities suggesting a transition from radical- to nitrogen oxide-limited regimes. OMI also observed the impact of reduced emissions during the 2020 COVID-lockdown resulting in increased FNRs.

1 Introduction

Tropospheric ozone (O_3) is a harmful pollutant which has detrimental impacts on air quality leading to adverse human health and premature mortality, and negative impacts on vegetation and agriculture (US EPA, 2006; Tai et al., 2014; GMD, 2020). A myriad of volatile organic compounds (VOCs) can be photochemically oxidized through a complex series of chemical reactions involving nitrogen oxides (NO_x = nitric oxide [NO] + nitrogen dioxide [NO_2]) which leads to tropospheric O_3 formation (Haagen-Smit, 1952; Monks et al., 2015; Seinfeld and Pandis, 2016). The complex O_3-NO_x-VOC chemical relationship results in local nonlinear O_3

formation which is sensitivity to the relative abundances of its precursor species (NO_x and VOCs), generally categorized as "NO_x-limited" versus "radical-limited" photochemical regimes (Sillman et al., 1990; Kleinman, 1994). In a NO_x-limited regime, local O_3 production increases/decreases with increased/reduced NO_x emissions and concentrations, with no impact from VOC perturbations. Whereas in a radical-limited regime (also known as "VOC-limited", "hydrocarbon-limited", or "NO_x-saturated") the formation of local O_3 increases/decreases with increased/reduced VOC emissions and concentrations; however, can also slightly be impacted by NO_x emission and concentration changes. The accurate knowledge of regional and local O_3 photochemical regimes is critical for developing emission control strategies to reduce surface O_3 concentrations. Overall, studying the spatiotemporal evolution of the nonlinear O_3-NO_x-VOC chemistry is critical to policy decision making (National Research Council, 1991) and important as a fundamental scientific problem (Sillman, 1999).

Diagnosing regional and local O_3 photochemical regimes has always been recognized as a challenging task. Measurements of proxy or indicator species (e.g., total reactive nitrogen, HCHO, hydrogen peroxide, nitric acid), and estimating the correlations of such species, are the observation-based or model-observation synthesis approaches to detect O_3 sensitivity regimes (Sillman, 1995; Jacob et al., 1995; Tonnesen and Dennis, 2000). These measurements and associated studies are typically limited to field campaign time periods and locations which hinders the spatiotemporal coverage of such data posing an obstacle for investigating global and regional O_3 production sensitivity over multi-year time periods. The response of O_3 formation to changes in precursor emissions can also be assessed through modeling approaches such as source apportionment studies (Li et al., 2012), forward model sensitivity simulations (Wu et al., 2009), and simulations using adjoint model capabilities (Zhang et al., 2009). However, uncertainties inherent in model predictions of O_3 physicochemical processes are a critical issue. Milford et al. (1994) and Sillman (1995) first introduced the concept of detecting photochemical regimes using the ratio of ambient concentrations of two "indicator species" HCHO to NO_2 (hereafter indicator species refers to HCHO and NO_2; the ratio of these two species as FNR), which can be used to represent VOCs and NO_x which are directly involved in O_3-NO_x-VOC chemistry and are readily measured via in situ sampling and satellite remote-sensing techniques. These two indicator species are the most suitable candidates for tropospheric column and planetary boundary layer (PBL) O_3 sensitivity analysis using satellites due to: 1) the sensitivity of nadir-looking satellites to boundary layer FNRs, 2) most other indicator species (e.g., hydrogen peroxide, VOCs other than HCHO) cannot be readily measured via satellites and the retrievals of those species having less sensitivity to surface conditions (e.g., limb-scanning satellites), and 3) the short atmospheric lifetime of HCHO and NO_2 allowing these species to be suitable for proxies of surface emissions of NO_x and VOCs.

Surface and PBL O_3 production sensitivity diagnosed with the in situ measurements of FNRs (although sparse in spatial and temporal coverage) should be more accurate compared to satellite-based approaches of retrieving column-integrated concentrations (Schroeder et al., 2017); however, the spatiotemporal coverage of polar orbiting satellites is a clear advantage over in situ techniques. The advancements in satellite remote-sensing over the last two decades, to retrieve HCHO and NO_2 vertical column density (VCD) data (Burrows et al., 1999; González Abad et al., 2019), have emerged as a new observation-based tool to detect the spatiotemporal evolution of O_3 sensitivity from a global- to local-scale (Martin et al., 2004; Jin et al., 2020). Martin et al. (2004) first demonstrated the capability of FNR VCDs from the Global Ozone Monitoring Experiment (GOME) satellite to detect photochemical regimes. Subsequently, this technique was adopted by more studies using other satellite instruments such as Ozone Monitoring Instrument (OMI), GOME-2, and TROPOspheric Monitoring Instrument (TROPOMI) (Duncan et al., 2010; Witte et al., 2011; Choi et al., 2012; Choi and Souri, 2015; Chang et al., 2016; Jin and Holloway 2015; Souri et al., 2017; Jin et al., 2017; 2020; Wang et al., 2021; Tao et al., 2022; Johnson et al., 2023; Acdan et al., 2023) up to a point that the results have been suggested to potentially be used to inform State-Implementation Plans (SIP) in the United States (US) (Jin et al., 2018). However, the accurate diagnosis of surface O_3 sensitivity regimes is impeded by numerous uncertainty components which can be

broadly classified into two major categories: 1) inherent uncertainties associated with the approach of relating indicator species to diagnose local O_3 sensitivity at a location/time period, and 2) uncertainties associated with satellite-retrieved column-integrated concentrations of indicator species to infer surface O_3 sensitivity. The former uncertainty arises from numerous factors: difficulties in identifying accurate FNR "threshold" values (hereafter, "threshold" refers to threshold ratio values) separating different O_3 sensitivity regimes over a location and time period (Schroeder et al., 2017; Jin et al., 2017), dependency of ambient O_3 and its formation to factors other than precursor species such as water vapor, meteorology, deposition, transport, and aerosol interaction (e.g., Kleinman et al., 2005; Camalier and Dolwick, 2007), varying sensitivity of HCHO VCD data to anthropogenic VOCs (Jin et al., 2020), and dependence of NO_2 in the production of ambient HCHO concentrations (Souri et al., 2020). These inherent uncertainty sources limit the utility of satellite-based data for diagnosing O_3 sensitivity regimes. Fortunately, recent studies have investigated these discrepancies in the methodology of using satellite-derived FNRs to infer O_3 sensitivity regimes using data from airborne campaign data and 0-D photochemical box models (e.g., Schroeder et al., 2017; Souri et al., 2020; Souri et al., 2023a).

This study investigates 17 years (2005-2021) of OMI satellite sensor data which provides consistent near daily global coverage of VCD retrievals of HCHO and NO_2 (Levelt et al., 2018) that are well suited to investigate the long-term spatiotemporal evolution of O_3 sensitivity regimes. Numerous studies have used OMI VCD data up to the year 2016 to assess the trends in FNR values over specific regions, mostly over the US and East Asia (Mahajan et al., 2015; Jin and Holloway, 2015; Souri et al., 2017; Jin et al., 2017, 2020). Extending the OMI data set out to 2021 is novel and allows for the investigation of COVID-19 lockdown restrictions on FNRs throughout the Northern Hemisphere. In this study we investigate the capability of VCD HCHO, NO_2, and FNR data from OMI to reflect the trends in PBL and surface level O_3 production sensitivity regimes. We do not calculate actual magnitudes of surface HCHO, NO_2, and FNRs derived with OMI VCD data as these proxy products are heavily reliant on chemical transport models (CTMs) and spatiotemporally sparse ancillary information, both sources which have large uncertainties (discussed in Sect. 4). Satellite retrieval errors can be reduced by averaging satellite data temporally (seasonal, annual, or multi-year means) and spatially (by averaging individual satellite pixels across 10's to 100's of kilometers), although such averaging approaches preclude the analysis of O_3 sensitivity regimes at high spatiotemporal scales. Several studies have therefore focused on assessing O_3 production sensitivity using spatially-averaged satellite data aggregated to monthly, seasonal, or multi-year means over large areas (e.g., Jin et al., 2020). In this study, we investigate the long-term changes in summer-mean (June, July, and August [JJA]) VCD FNRs across numerous polluted cities (cities with high NO_2 VCDs) in the Northern Hemisphere. This manuscript is structured in the following way. Section 2 describes the OMI retrievals, surface concentration measurements, "bottom-up" emission inventories, and the approach to conduct spatiotemporal variability and trend analysis. In Sect. 3, we describe the comparison of satellite VCD FNRs to surface measurements and the analysis of OMI-derived FNR values over Northern Hemisphere cities. Section 4 discusses the capabilities and issues with applying satellite-derived FNRs for studying O_3 production sensitivity and concluding remarks are provided in Sect. 5.

2. Materials and methods

2.1 OMI satellite sensor

The OMI sensor is a Dutch-Finnish built payload on the NASA Earth Observing System Aura satellite. The Aura platform flies as part of the Afternoon-Train satellite constellation along a sun-synchronous polar Low Earth Orbit (Schoeberl et al., 2006). Aura passes through the sunlit part of the Earth 14 times a day with a local overpass time of ~1:45 p.m. at the equator with near-complete daily global coverage (Levelt et al., 2006). OMI is a nadir-viewing solar backscatter grating spectrograph which takes retrievals in the ultraviolet (264–311 nm [UV1] and 307–383 nm [UV2]) and visible (349–504 nm) wavelengths (Levelt et al., 2006, 2018; Schenkeveld et al., 2017). The OMI instrument has a swath width of 2,600 km (60 pixels across track) with near-nadir spatial

117 resolution of 13 km (along-track) × 24 km (cross-track) and near-swath edge pixel size of 40 km × 250 km. OMI has been widely
118 used by the atmospheric science, air quality, and health impact assessment communities since its launch on July 15, 2004 (e.g.,
119 Levelt et al., 2018). The "row anomaly" appeared starting in May 2007 affecting the data quality of certain rows of OMI pixels
120 (Dobber et al., 2008, Schenkeveld et al., 2017) and is avoided in the data products used in this study.

2.1.1 OMI HCHO

122 This study applies the NASA-released operational OMI HCHO version 3 collection 3 (OMHCHO) gridded level 3 (L3) VCD data
123 at a spatial resolution of $0.1° × 0.1°$ latitude × longitude using the Smithsonian Astrophysical Observatory (SAO) retrieval
124 algorithm (González Abad et al., 2015). The OMHCHO retrieval applies a nonlinear fitting to the OMI-measured backscattered
125 radiances in the UV2 spectral window following the Basic Optical Absorption Spectroscopy method (Chance, 1998) to get slant
126 column densities (SCDs). The SCDs are then converted to VCDs by applying the air mass factor (AMF) formulation of Palmer et
127 al. (2001), with scattering weights calculated using the Linearized Discrete Ordinate Radiative Transfer version 2.4RT (VLIDORT)
128 Radiative Transfer Model (RTM) (Spurr, 2006) and HCHO shape factors simulated using the GEOS-Chem global CTM at a spatial
129 resolution of $2° × 2.5°$ latitude × longitude. The OMHCHO VCD product has a postprocessing bias correction (De Smedt et al.,
130 2008) applied by comparing daily HCHO VCDs with background VCDs simulated with GEOS-Chem over a clean region in the
131 Pacific Ocean (González Abad et al., 2015). González Abad et al. (2015) estimated the uncertainty of the OMHCHO product
132 ranging from 45% to 105%, with relative contributions from the slant column retrievals (45% – 100%) and AMF calculations
133 (~35%). Model evaluation studies have shown that CTMs have errors and uncertainties in their predictions of HCHO in the clean
134 regions of the Pacific Ocean which could also contribute to overall OMI HCHO bias/errors (Anderson et al., 2017). Validation of
135 OMHCHO with aircraft-based observations indicates a high bias (66.1% – 112.1%) for HCHO-poor environments and low bias (-
136 44.5% – -21.7%) for HCHO-rich environments (Zhu et al., 2016, 2020; Johnson et al., 2023). The OMHCHO product has been
137 used widely for estimating trends of VOC emissions (e.g., Marais et al., 2012; Shen et al., 2019) and inferring surface HCHO
138 concentrations (Zhu et al., 2017a).

2.1.2 OMI NO$_2$

140 The NASA-released standard OMI NO$_2$ (OMNO2) version 4 collection 3 gridded L3 high resolution VCD data at the spatial
141 resolution of $0.1° × 0.1°$ latitude × longitude was applied in this study (Lamsal et al., 2015; Krotkov et al., 2017). The OMNO2
142 retrieval uses the Differential Optical Absorption Spectroscopy method (Marchenko et al., 2015) to derive tropospheric SCDs by
143 spectrally fitting OMI-detected backscattered radiance in the visible wavelength window with a pseudo reference spectrum
144 (Chance and Spurr, 1997). The stratospheric contribution of the SCD is then subtracted and the residual tropospheric SCDs are
145 then converted to tropospheric VCDs by applying an AMF based on scattering weights calculated using the Total Ozone Mapping
146 Spectrometer (TOMS) radiative transfer model (TOMRAD) (Dave, 1964) and shape factor profiles simulated using the Global
147 Modeling Initiative (GMI) CTM at a spatial resolution of $1° × 1.25°$ latitude × longitude (Krotkov et al., 2017). The uncertainty of
148 the OMNO2 VCD product varies with cloudiness and pollution levels but is in the range of ~20% – 60% (Bucsela et al., 2013),
149 with relative contributions from the spectral fitting (~10% over polluted regions, Boersma et al., 2011), stratospheric correction
150 (<5%), and AMF calculations (10% – 20%). The OMNO2 product has been used for a wide range of applications including the
151 estimation of spatiotemporal variability and trends of NO$_x$ emissions (e.g., Krotkov et al., 2016), NO$_2$ surface concentrations (e.g.,
152 Kharol et al., 2015; Lamsal et al., 2015), information about atmospheric particulate organic matter (Philip et al., 2014), and surface
153 O$_3$ sensitivity regime detections (e.g., Duncan et al., 2010; Jin et al., 2017).

2.1.3 Calculation of VCD FNR values

The daily L3 OMHCHO and OMNO2 products were filtered and processed for calculating FNR values. Both the operational products were already filtered for daily VCDs with an effective cloud fraction >30%, solar zenith angle >70% (for HCHO) and >85% (for NO_2), removing pixels affected by row anomalies, and Level 2 data quality flags not designated as good (see more details in the user's guides for OMNO2 [https://disc.gsfc.nasa.gov/datasets/OMNO2d_003/summary] and OMHCHO [https://acdisc.gesdisc.eosdis.nasa.gov/data/Aura_OMI_Level3/OMHCHOd.003/doc/README_OMHCHOd_v003.pdf]).

During this study, we avoided unrealistically large positive and negative values for both indicator species which occur due to uncertainties in slant column retrievals and the calculation of tropospheric VCDs. We followed Zhu et al. (2020) to filter out HCHO daily VCDs outside the range of -8.0×10^{15} molecules/cm^2 to 7.6×10^{16} molecules/cm^2. The OMNO2 L3 product already included an upper limit of 1×10^{17} molecules/cm^2 and we applied a lower limit of -1×10^{15} molecules/cm^2 below which NO_2 VCD are assumed in this study to be unrealistic. After data filtering, OMI VCD FNRs are calculated by taking the ratio of HCHO:NO_2 for each grid of the summer-mean products.

2.2 Surface measurement data

To determine if OMI VCD FNRs can replicate the trends of PBL and surface-level FNRs, long-term trends in OMI-derived VCD HCHO and NO_2 are compared to in situ measurement data from the United States Environmental Protection Agency's Air Quality System (US EPA AQS; https://www.epa.gov/aqs). We focus this evaluation on the US due to the much denser in situ measurement networks compared to other global regions. Hourly data from the EPA AQS NO_2 data were averaged daily from 1 pm to 3 pm local time to be consistent with the OMI overpass time. Since there is insufficient hourly data for HCHO from the EPA AQS network, we use 24-hour average data for the HCHO evaluation which is provided by the EPA. AQS data for HCHO and NO_2 from each site are only used for days in which both species are measured. Valid and continuous data points were then averaged to obtain seasonal summertime mean (JJA) values from 2005 to 2019 to be intercompared with corresponding OMI VCD values.

The AQS NO_2 data suffers from potential interference of reactive nitrogen species while measuring NO converted from NO_2 in molybdenum catalytic converters, since other reactive species also get converted to NO. We attempted to account for this interference by applying a model simulated correction factor (CF; Eq. 1) to the raw AQS data, following the approach of previous studies (Lamsal et al., 2008; 2010; Cooper et al., 2020).

$$CF = \frac{NO_2}{NO_2 + (0.15 \times HNO_3) + (0.95 \times PAN) + \text{Alkyl Nitrates}} \tag{1}$$

The CF is calculated using the MERRA2-GMI simulated concentrations of NO_2, HNO_3, peroxyacetyl nitrate (PAN), and alkyl nitrates, and by applying an assumed effective conversion efficiency of 15% for HNO_3 and 95% for PAN (see Lamsal et al., 2010). The AQS's method to measure HCHO is affected by interference from species such as O_3 and NO_2 and since there is insufficient information to correct those interferences, here we use uncorrected AQS HCHO data.

2.3 Surface emissions of NO_x

To compare the long-term evolution of FNRs with human-induced changes in precursor emissions (anthropogenic emissions of NO_x), we used the most recent Community Emissions Data System (CEDS v_2021_04_21) NO_x bottom-up emission data set (McDuffie et al., 2020). As explained in the results section of this manuscript, we focus our analysis on trends in NO_x emission instead of HCHO as it was determined that trends in NO_2 concentrations clearly drive the global trends in FNRs. The CEDS data provides monthly anthropogenic NO_x emissions at $0.5° \times 0.5°$ horizontal spatial scales from $1750 - 2019$. For this study we analyse trends in anthropogenic NO_x emissions (source sectors: Agriculture; 1: Energy; 2: Industrial; 3: Transportation; 4: Residential,

Commercial, Other; 5: Solvents production and application; 6: Waste; 7: International Shipping) between 2005 – 2019 to overlap with OMI observations. We used mean emissions for summer months (JJA) for each year to intercompare with OMI derived NO_2 and FNR trends. Since our focus in this study was to assess the overall relationship of long-term changes in OMI-derived FNR values and corresponding changes in the anthropogenic NO_x over a city/region, we do not consider other natural sources (e.g., biomass burning) contributing to ambient concentrations of urban NO_2.

2.4 Spatiotemporal analysis of FNRs

The spatiotemporal analysis of OMI-derived VCD NO_2 and HCHO values was conducted as follows. First, summer-mean trends from 2005 to 2021 of HCHO and NO_2 VCDs and FNR values were calculated at the native spatial resolution ($0.1° \times 0.1°$). Long-term trends were calculated for each grid of HCHO, NO_2, and FNRs with ordinary least-squares linear regression (at various confidence levels calculated with the Mann-Kendall Test) similar to past studies (e.g., Boys, et al., 2014; Kharol et al., 2015; Geddes et al., 2016). To reduce retrieval random errors and improve precision, we focus on summer-mean data for each year and multi-year means (three multi-year means: 2005 – 2010, 2011 – 2015 and 2016 – 2021) around 46 cities across the Northern Hemisphere. The focus on the summer season was also chosen to utilize HCHO VCD retrievals with significantly better signal to noise ratios compared to winter, spring, and fall months. High levels of surface HCHO concentrations over source regions form due to the higher oxidant availability in summer (González Abad et al., 2015; Zhu et al., 2014; 2017a; 2017b) which leads to better retrievals of HCHO VCDs. We restrict our analysis to the Northern Hemisphere as most continental polluted regions exist there. We assessed the evolution of FNRs over urban and rural/suburban (hereinafter referred to just as rural) areas around cities. To define urban city regions, we used the hybrid dataset, CGLC-MODIS-LCZ (Demuzere et al., 2023), which is based on the Copernicus Global Land Service Land Cover (CGLC) product resampled to MODIS IGBP classes (CGLC-MODIS) and the global map of Local Climate Zones (LCZ) (Stewart and Oke., 2012) that describe the heterogeneous urban land surface. This data set was interpolated onto a $0.1° \times 0.1°$ grid to match the resolution of the L3 OMI satellite data. Urban classification is defined by the CGLC-MODIS-LCZ land use categories 51 – 60, which includes a range of urban land use from sparely built to compact high-rise including the heavy industry category. These land use categories capture both urban and suburban landscapes. Rural grids are those not defined as urban and within 7×7 grid boxes of the city center. The CGLC-MODIS-LCZ urban and rural maps derived for this study are static and will not capture urban expansion which has occurred over the last two decades. However, since our urban classification includes both urban and suburban landscapes (including sparsely built-up areas), the transition from suburban to urban landscapes will already be included in our urban map. The only thing not captured would be the transition from completely vegetative areas to more built-up landscapes which are expected to have a minor impact on the results of this study.

In this study, we focus only on the spatiotemporal variability of indicator ratios, rather than the exact ozone sensitivity regimes which can be inferred from these ratios. Although several previous studies assigned ratio values to certain O_3 regimes (e.g., Jin et al., 2017; Souri et al., 2017) based on previous modelling and limited-observational studies, large uncertainty exists in the classification of O_3 regimes using FNR values (Schroeder et al., 2017; Jin et al., 2020; Souri et al., 2021). Nevertheless, whenever the ratio values were assessed over a city/region, we also presented the threshold ratio values (separating O_3 regimes) suggested by Jin et al. (2020) for some cities in the US (Los Angeles, New York, Chicago, Washington DC, Pittsburgh, Atlanta and Houston), Wang et al. (2021) for cities in China, and Duncan et al. (2010) for all other cities/regions. Note that the threshold FNR values (< 1 as radical-limited versus > 2 as NO_x-limited) suggested by Duncan et al. (2010) is a crude approximation as opposed to more recent and observationally-constrained threshold ratio values suggested by Jin et al. (2020) and Wang et al. (2021). We believe that an accurate classification of O_3 regimes is still an ongoing research topic (Schroeder et al., 2017; Jin et al., 2020; Souri et al., 2021) which should be addressed in future studies.

3. Results

3.1 Long-term mean OMI data

Figure 1 shows the long-term mean (2005-2021) maps of OMI-derived VCDs of HCHO and NO_2 and the corresponding column FNR values. Formaldehyde enhancements reflect surface emissions of anthropogenic VOC (densely populated regions in China; Shen et al., 2019), biogenic isoprene (southeast US; Millet et al., 2008), and biomass burning (South Asia; Mahajan et al., 2015). OMI VCD NO_2 is abundant over urban areas primarily due to fossil fuel combustion emissions from traffic (Duncan et al., 2015) and over regions with large industrial activities (Krotkov et al., 2016). The column FNRs clearly reveal lower values over cities (FNR < 2), marginal values over rural/suburban regions surrounding large cities (FNR in the range of 2 - 5), and higher values elsewhere (FNR > 5). The lower FNRs over cities suggest radical-limited conditions, and larger FNR values in non-polluted background regions reflect NO_x-limited conditions (Martin et al., 2004; Duncan et al., 2010; Jin et al., 2017; 2020; Wang et al., 2021). Lower FNR values retrieved by OMI are most noticeable in the highly populated regions of the US (e.g., Los Angeles, New York, Chicago), Europe (e.g., London, Amsterdam, Paris), East Asia (e.g., Beijing, Shanghai, Jinan), and Middle East (e.g., Dubai, Tehran, Riyadh) where tropospheric column NO_2 abundances are enhanced. The highest FNR values are observed in regions of the southeast US and south Asia (e.g., Malaysia) where there are no large cities and enhanced tropospheric column HCHO abundances, primarily from biogenic emissions, are observed.

3.2 Capability of OMI VCD data to observe surface-level FNR trends

Before assessing VCD FNR trends, we compared trends in OMI NO_2 and HCHO VCD data, and corresponding tropospheric column FNRs, to surface in situ measurements from EPA AQS in the US in order to determine whether OMI VCD information tracks trends occurring at the surface. Figure 2 shows the 15-year time-series (2005-2019) comparison between normalized time series of OMI VCD indicator species abundances and FNRs and AQS data over select cities (US cities with continuous AQS data), and over all cities averaged across the continental US (USA, 373 separate sites). Table 1 shows the correlation between OMI VCD and AQS in situ NO_2, HCHO, and FNR summer mean values in addition to the simple linear regression slope of normalized trends from OMI and AQS for both indicator species and FNRs. Figure 2 shows that both OMI VCD and in situ AQS data have relatively neutral trends in HCHO between 2005 and 2019 for most of the large urban cities of the US. While there is large interannual variability in HCHO concentrations, the long-term trends are relatively flat. On average, the normalized linear trends in surface HCHO in urban regions of the US was -0.05 yr^{-1} and OMI VCDs was +0.15 yr^{-1}. OMI VCD HCHO data is unable to replicate the interannual variability and long-term trends of surface data displayed by the low correlation values and opposing trends in multiple large cities in the US. The inability of OMI to reflect the variability in HCHO observed at the surface is likely due to the coarse spatial resolution of the OMI footprint, large noise in OMI HCHO retrievals (e.g., Johnson et al., 2023, Souri et al., 2023a), and complex vertical distributions of HCHO complicating satellite retrievals and representation of surface values (e.g., Souri et al., 2023b).

OMI VCD and in situ AQS data of NO_2 display a different story where statistically significant reductions at a 95% confidence level in NO_2 concentrations are observed by both data sources. The normalized trends in NO_2 from both measurement platforms are in strong agreement (see Fig. 2 and Table 1). Correlation between OMI VCD and AQS NO_2 was near 1.0 (R=0.98) and both data sources had normalized linear regression slopes of ~-0.20. This suggests that OMI is able to observe the strong reduction in NO_2 concentrations at the surface measured by AQS across the US. Both data sources suggest that NO_2 reduced between 2005-2019 and the strongest negative trends were in the large cities of the US such as New York, Chicago, and Los Angeles. The near neutral trend in HCHO and large decreases in NO_2 results in both OMI VCD and in situ data sources observing

268   an increasing trend in FNR data in all major cities of the US shown in Fig. 2. The normalized linear regression trend slopes of

269   FNRs (0.21 from both OMI and AQS data) are all statistically significant reductions at a 95% confidence level and are nearly equal

270   and opposite to NO_2, suggesting the reduction of NO_2 is the primary driver of FNR trends over time. It is encouraging that OMI

271   VCD data is able to accurately reproduce the normalized trends in surface FNRs in the US. This agrees with the recent studies

272   from Jin et al. (2017) and Souri et al. (2023a) which show that ratios of mid-day tropospheric VCD FNRs to PBL and surface-

273   level concentrations are near unity. Since OMI VCD FNRs appear to be able to replicate the trends in surface FNRs, the rest of

274   this study focuses on the trends of FNRs from OMI VCD data for the Northern Hemisphere.

275   **3.3 17-year trend in OMI observations**

276   This study investigates the 17-year trend of OMI VCD of HCHO, NO_2 and FNR values between 2005 and 2021. Figure 3 shows

277   the long-term trend in OMI VCD HCHO, NO_2 and FNR values at an 85% confidence level ($p \le 0.15$) (Fig. S1 shows the same

278   trend values at a 99% [$p \le 0.01$] confidence level and for all grid cells with OMI retrievals). The same information shown in Fig.

279   3 is displayed individually for North America, Europe, and Asia in the supplemental information (see Fig. S2). Formaldehyde

280   VCDs increased by ~0.5×10^{14} molecules cm^{-2} yr^{-1} over most of the Northern Hemisphere, with reductions up to ~-0.5×10^{14}

281   molecules cm^{-2} yr^{-1} over the southeast US. This trend is consistent with previous studies documenting increases in multi-satellite

282   (including OMI) summer mean HCHO over Northern China (during 2005-2016 [Shen et al., 2019] and 2005-2014 [Souri et al.,

283   2017]) and increases in most regions in the US (during 2005-2014 [Zhu et al., 2017b]) due to increasing anthropogenic VOC

284   emissions. Some near neutral trends, to small decreases, are seen in Fig. 3 in eastern China. The decrease in HCHO over Southern

285   China could be due to reductions in anthropogenic VOCs (Souri et al., 2017; Itahashi et al., 2022) or biogenic VOC emissions as

286   noted by Jin and Holloway (2015). The decreases in summer mean OMI HCHO over the southeast US were also documented in

287   earlier studies (De Smedt et al. 2015; Zhu et al., 2017b). Note that the trend in HCHO calculated in this study is influenced by

288   yearly variations in temperature, in contrast to Shen et al. (2019) and Zhu et al. (2017b) that corrected for the impact of varying

289   temperature on HCHO VCDs.

290   It should be noted that the NASA-released operational OMI HCHO version 3 collection 3 data product used in this study

291   has been shown to have a positive drift due to instrument aging (e.g., Marais et al., 2012; Zhu et al., 2014, 2017b). This positive

292   trend in OMI HCHO data displayed in Fig. 3 is likely largely impacted by the artificial positive drift in the collection 3 OMI data.

293   A new NASA OMI HCHO version 3 collection 4 product is in development using the SAO algorithm which has removed this

294   positive drift in HCHO (Ayazpour et al., 2024; personal communication with the SAO HCHO algorithm team). This new HCHO

295   retrieval product shows that HCHO has a near-neutral trend across most of the populated cities in the Northern Hemisphere. This

296   new collection 4 retrieval data is not yet peer-reviewed or available to the public therefore is not used here and the remaining

297   results in this study use OMI HCHO version 3 collection 3 data. However, to test the potential impact on the results of this study

298   using an OMI VCD product with this average positive drift eliminated, we removed the mean annual Northern Hemispheric HCHO

299   trend (~0.004 DU yr^{-1}) from the collection 3 data and evaluate the resulting FNR trends over 18 selected large cities in the Northern

300   Hemisphere which is discussed in Sect. 3.4.

301   The negative trend in NO_2 OMI VCDs over populated regions of the US, Europe, and eastern China, and increases in the

302   South Asia and Middle East regions, seen in Fig. 3 are consistent with several previous studies (e.g., Hilboll et al., 2013; Jin et al.,

303   2017). The decreases in eastern China and Europe are as large as -2.0×10^{14} molecules cm^{-2} yr^{-1} while reductions in NO_2 in the

304   US are between -0.1 to -1.0×10^{14} molecules cm^{-2} yr^{-1}. The decreasing NO_2 trend in eastern China could be due to recent reductions

305   in anthropogenic NO_x emissions after year 2011 (e.g., Fan et al., 2021). It is well demonstrated that the tropospheric NO_2 decreases

306   in most Northern Hemisphere regions, particularly in urban regions, is due to reductions in anthropogenic NO_x emissions

307   implemented through national governmental policies (e.g., Duncan et al., 2016; Koplitz et al., 2021). Figure S3 shows the trends

308   in CEDS anthropogenic NO_x emissions between 2005-2019 which have nearly identical regions of reduction as those retrieved by

309   OMI NO_2. Overall, the summer-mean trend in VCD NO_2 estimated in this study is generally consistent with the reported satellite-

310   based annual mean surface NO_2 trend estimated on a global-scale (Geddes et al., 2015) and over the US (Kharol et al., 2015;

311   Lamsal et al., 2015).

312   The most notable feature in Fig. 3 is the general increasing trend in OMI VCD FNR values over most of the polluted

313   regions in the Northern Hemisphere. The increasing OMI column FNR values suggest a trend towards more NO_x-limited regimes

314   around cities in recent years which has been noted by some previous studies (Jin et al., 2017; 2020; Souri et al., 2017). Increases

315   in FNRs in the populated regions of China, Europe, and US reach values between 0.1 and 0.2 yr^{-1}. The increases in FNRs are

316   driven mostly by the reductions in NO_2 rather than the small variations in HCHO, as evident in Fig. 2 and 3. The following sections

317   focus on the assessment of the evolution of summer mean OMI-derived VCD FNRs over numerous selected cities in the Northern

318   Hemisphere.

319   **3.4 Evolution of OMI FNRs around populated cities in the Northern Hemisphere**

320   Figure 4 shows the time series of summer mean OMI VCD FNRs from 2005 to 2021 over 18 selected large cities. The

321   corresponding normalized time series trends of OMI-derived NO_2 abundances and FNRs, and CEDS anthrophonic emissions of

322   NO_x over these cities, are displayed in Fig. 5. From Fig. 4 it can be seen that the largest positive trends in OMI FNRs during the

323   2005-2021 time period occurred over three mega-cities in the US: Los Angeles, New York and Chicago. Time series of the actual

324   magnitudes of OMI VCD NO_2 and HCHO abundances over the selected 18 large cities are shown in Fig. S4. In addition to increases

325   in FNRs in US cities, relatively large increases in FNRs are also evident in European (e.g., London) and Asian (e.g., Guangzhuo)

326   cities. To test whether the positive drift in the NASA OMI HCHO collection 3 data significantly impacted the results of the FNR

327   trends over the 18 selected large cities in the Northern Hemisphere we present these same results in Fig. S5 with the OMI data

328   which has the annual average Northern Hemispheric HCHO trend remove (more representative of OMI HCHO version 3 collection

329   4 data) and Fig. S6 shows the spatial trends of HCHO, NO_2, and FNRs over the Northern Hemisphere using this detrended HCHO

330   data. Comparing Figs. S5 and 4, it is seen that while some of the FNR values are slightly lower in magnitude the positive trends

331   are very similar using collection 3 HCHO retrievals and a data product with the positive drift removed. Throughout the Northern

332   Hemisphere HCHO trends now display both positive and negative values (see Fig S6) instead of the constant positive trends from

333   the OMI HCHO collection 3 product. Using the detrended OMI HCHO data does result in more negative FNR trends in remote

334   regions outside of large urban regions; however, over urban areas, and rural regions surrounding large cities, the FNR trends are

335   still positive as displayed in Fig. S5 and S6. Overall, using the OMI HCHO version 3 collection 3 data product does not significantly

336   impact the FNR results in large cities in the Northern Hemisphere focused on in this study. Future studies investigating FNRs

337   conducted when the NASA OMI HCHO version 3 collection 4 data is available to the public should however use this new product

338   to present more accurate results compared to those shown here using the NASA OMI HCHO version 3 collection 3 product.

339   Figure 5 reveals that the increases in OMI FNR values over the selected 18 mega-cities are linked with decreases in NO_2

340   abundances due to reductions in anthropogenic NO_x emissions. The spatial map of trends in CEDS anthrophonic emissions of NO_x

341   across the Northern Hemisphere between 2005-2019 are shown in Fig. S3 (timeseries of CEDS NO_x emission magnitudes for the

342   selected 18 mega-cities shown in Fig. S7). Based on the O_3 production sensitivity regime thresholds suggested by Jin et al. (2020)

343   (note that these thresholds are applicable for VCD data), all the US cities shown in Fig. 4 that were VOC-limited in the early 2000's

344   show clear transition towards NO_x-limited and transitional regimes in recent years. Major cities in Europe such as London and

345   Amsterdam have also experienced increasing FNRs moving from VOC-limited regimes to transitional, or even NO_x-limited,

regimes in recent years (based on thresholds from Duncan et al. [2010]). Increases in the magnitudes of FNRs were generally smaller in large cities of Asia; however, only Neijiang doesn't display some noticeable increases in FNRs in recent years. In Neijiang, CEDS anthropogenic NO_x emissions are decreasing after 2012; however, OMI does not retrieve decreasing NO_2 abundances leading to the near-neutral trend in FNR values. Based on the O_3 production sensitivity regimes thresholds defined by Wang et al. (2021) and Duncan et al. (2010), major cities in Asia have FNR values which are in the transitional or NO_x-limited regimes in recent years besides Beijing, Shanghai, Jinan, and Riyadh (surrounding rural region is in the transitional regimes) (see Fig. 4). Figure 5 shows these large Asian cities, besides Riyadh, implemented NO_x emission control strategies in ~2012 and have recent negative trends in OMI NO_2; however, based on Wang et al. (2021) these urban regions have O_3 production which is still limited by VOCs. Overall, it is difficult to conclude if these major cities in the Northern Hemisphere have in fact transitioned to NO_x-limited and transitional regimes due to the large uncertainties in the exact threshold FNR values which separate these chemical regimes.

In the vast majority of cities between 2005-2021 OMI retrieved larger FNR values in the rural regions surrounding urban regions in the Northern Hemisphere compared to the urban city centers. Figure 6 shows spatial maps of OMI-derived VCD FNRs around the selected 18 cities discussed above for two 6-year averages: 2005-2010 and 2015-2021 reflecting the earliest and most recent years of OMI data studied here. The spatial maps of OMI-derived HCHO and NO_2 VCD values for these same time periods over the 18 cities are displayed in Fig. S8 and S9, respectively. Figure 6 shows that OMI is able to retrieve the differences in FNRs in urban and rural regions surrounding large cities in the Northern Hemisphere (Fig. S10 shows the same information in Fig. 6 except with the CGLC-MODIS-LCZ urban grids used to separate urban and rural values). In urban areas of cities, where emission sources of NO_x are largest, OMI FNRs tend to be lower indicating more tendency towards VOC-sensitive O_3 production regimes compared to the surrounding rural regions. This figure also displays the decadal-scale changes (2016–2021 versus 2005–2010) in the OMI FNRs over the Northern Hemisphere urban regions and surrounding rural regions. In all 18 cities FNR values increase in both rural and urban areas with noticeable increases in the spatial coverage of potentially NO_x-limited O_3 production regimes. These spatial distributions of increasing FNR values retrieved by OMI are clearly correlated with decreasing tropospheric NO_2 over the vast majority of cities displayed in Fig. S9. Large cities in the US show the clearest increase in the spatial coverage of potentially NO_x-limited O_3 production regimes; however, European and Asian cities also follow a similar pattern with less increase in FNR magnitude overall. Recent studies have also noted that NO_x-limited regimes have expanded spatially into the city centers, on a decadal-scale, throughout the Northern Hemisphere (Jin et al., 2017) and in the US (Jin et al., 2020). This has large implications for O_3 sensitivity analysis and development of future emission control strategies for improving air quality.

Figure 7 shows the changes in OMI FNRs (multi-year averaged values: 2005-2010, 2011-2015, and 2016-2021) over 46 cities in the Northern Hemisphere. The vast majority of urban regions in the Northern Hemisphere (44 of the 46 selected cities) experienced increasing FNRs between 2005-2010 and 2016-2021. OMI FNRs for Tehran, Iran and Neijiang, China were two selected cities which did not display increasing values. On average, FNRs in urban areas of the selected cities increased by ~65% between 2005-2010 and 2016-2021. Similar to urban regions, the vast majority of rural regions surrounding urban areas in the Northern Hemisphere (44 of the 46 selected cities) experienced increasing FNRs between 2005-2010 and 2016-2021. The average increase of FNRs in the rural regions increased slightly less (~38%) compared to urban areas. In agreement with results discussed above, FNR values in rural regions are larger compared to city centers. However, OMI VCD FNR differences between rural and urban regions were reduced by ~15% on average over the 17-year time period. This suggests that the urban/rural interface of FNRs is becoming less drastic and NO_x-limited O_3 production regimes that in the past were predominantly observed in rural regions have expanded into the urban regions of larger cities. More accurate assessment of the actual threshold ratio values separating the different O_3 production regimes would allow for the determination of exactly what extent of each city has in fact transitioned to

NO$_x$-limited regimes. Overall, Fig. 7 demonstrates that the long-term record of OMI observations can observe the impact of global emissions reduction strategies on air quality and O$_3$ sensitivity regimes throughout the Northern Hemisphere.

3.5 Impact of the COVID-lockdown on FNRs in the Northern Hemisphere

The global impacts of the COVID-lockdown in 2020 on atmospheric pollution, such as the reduction of tropospheric NO$_2$, has been well documented to have impacted O$_3$ sensitivity regimes in the PBL and mid- to upper-troposphere (e.g., Goldberg et al., 2020; He et al., 2020, Cooper et al., 2022; Nussbaumer et al., 2022). Here we studied, for the first time, OMI derived VCD FNRs to evaluate the impact of the COVID-lockdown on summer-mean FNRs in 2020 throughout the Northern Hemisphere compared to the year before (2019) and after (2021). Figure 8 shows the changes in OMI FNRs before, during, and after (2019, 2020, 2021) the COVID-lockdown over the selected 46 cities discussed in this study. Out of the 46 selected cities, 32 of the urban regions (~70%) experienced higher FNRs in 2020 compared to 2019. On average, the cities that experienced increased FNRs in 2020 had values which were ~19% higher compared to 2019. Similarly, 26 of the urban regions (~57%) experienced higher FNRs in 2020 compared to 2021 and these city centers had FNR values ~18% larger. OMI also retrieved increased FNR values in rural regions surrounding city centers throughout the Northern Hemisphere during the COVID-lockdown period of 2020 (see Fig. 8). A similar number of city's rural areas experienced increased FNRs in 2020 compared to 2019 and 2021 as what was observed for urban areas. The increases in FNRs for rural regions in 2020 compared to 2019 and 2021 were 16% and 13%. The OMI data evaluated here suggest that the majority of cities in the Northern Hemisphere, and surrounding rural regions, tended to have O$_3$ production which was more sensitivity to NO$_x$ emissions/concentrations in 2020 compared to the year before and after. Cooper et al. (2022) demonstrated that in 2020 NO$_2$ concentrations were on average ~30% lower during COVID-lockdown periods and these reductions were from decreased anthropogenic emissions and can't be explained by meteorological differences. The degree of reduction in NO$_2$ determined in Cooper et al. (2022) agrees well with the OMI VCD FNR increases determined during our study of ~20%.

3.6 Comparison of OMI and TROPOMI FNR spatiotemporal variability in US cities

To expand upon previous studies which investigated OMI FNR trends published prior to the availability of TROPOMI retrievals (e.g., Mahajan et al., 2015; Jin and Holloway, 2015; Souri et al., 2017; Jin et al., 2017, 2020), here we compare the ability of OMI and TROPOMI to reproduced inter-city and interannual FNR variability in the US measured by EPA AQS sites in the 7 major US cities illustrated in Fig. 2. For this purpose, we applied TROPOMI operational Royal Belgian Institute for Space Aeronomy (BIRA) L2 HCHO version 2.4.1 and Dutch OMI NO$_2$ data products of KNMI for OMI (DOMINO) NO$_2$ version 2.4 retrievals interpolated to a standardized $0.1° \times 0.1°$ grid format. Figure 9 shows the normalized summer mean FNRs (city-specific annual FNR values normalized by the 7-city FNR mean) for the 7 selected US cities for 2018 and 2019. For both years, TROPOMI was able to reproduce the inter-city variability in normalized AQS FNRs with better agreement compared to OMI for 5 of the 7 US cities. This is further emphasized by the fact that TROPOMI reproduced 48% and 93% of the inter-city FNR variance (R^2) measured by AQS data for 2018 and 2019, respectively, while OMI only reproduced ~30% of the FNR variability measured in both years. Furthermore, TROPOMI more closely reproduced the direction of change in AQS measured FNRs between 2018 and 2019 for 6 of the 7 cities (85%) while OMI was only able to reproduce the FNR differences for 3 of the 7 cities (43%). The improved capability of TROPOMI to capture spatiotemporal FNR variability compared to OMI is to be expected as recent studies have demonstrated improved HCHO and NO$_2$ retrievals from the newer and higher spatial resolution sensor (e.g., Souri et al., 2023a; Johnson et al., 2023) and OMI is far past the expected lifetime of the sensor. Future studies should intercompare the two sensor's retrievals of FNRs for the entire lifetime of TROPOMI which overlaps with OMI (2018-present) to fully understand the improvements when applying TROPOMI.

4. Discussing the use of OMI data to assess O₃ production sensitivity regimes

The OMI satellite sensor offers a continuous data record across the globe with sufficient spatiotemporal resolution to assess tropospheric O_3 production sensitivity which cannot be achieved with in situ observations. The analysis in this study demonstrated that the 17-year record of OMI-retrieved HCHO and NO_2 data offered an unprecedented opportunity to assess the long-term evolution of VCD, and likely surface-level, FNR values, with potential future applications in linking these ratio changes with changes in surface O_3 regimes. Here we show that OMI VCD data of FNRs replicate the trends observed with surface in situ information. In order to produce actual satellite-derived surface values of HCHO, NO_2, and FNRs using VCD retrievals requires algorithms which largely depend on CTM-predicted vertical distributions of these trace gases (e.g. Zhu et al., 2017a; Jin et al., 2017; Cooper et al., 2020). Surface-based and aircraft in situ observations are also used for this purpose; however, these observations have minimal observational coverage due to being very spatiotemporally limited (e.g., Souri et al., 2023a). Using model simulations or in situ data to convert satellite VCD information to surface-level HCHO, NO_2, and FNRs concentrations are both inhibited by errors. In situ observations are too sparse and CTMs have system-specific errors/biases and differ largely in their prediction of HCHO and NO_2 vertical distributions (Lamsal et al., 2008; Geddes et al., 2016; Souri et al., 2023b). This results in large uncertainties in surface-level FNRs when convolving satellite VCDs. Our study does not address the conversion of OMI VCDs to surface-level values, but clearly shows that this spaceborne sensor can capture the trends in surface-level FNRs. The ability of VCD information from low earth orbit satellites to capture mid-day surface-level FNR trends might be due to studies showing ratios of VCD FNRs to PBL/surface values are near unity (Jin et al., 2017; Souri et al., 2023a). However, during times where HCHO and NO_2 vertical profiles in the troposphere are not similar to climatological averages, models and satellites may be challenged to accurately assess conversion ratios of VCD FNRs to PBL/surface values (e.g., Souri et al., 2023b). Overall, if methods are improved to reduce the uncertainty in the conversion of satellite VCD retrievals of HCHO and NO_2 to surface-level concentrations, then satellite-derived surface-level FNRs will be able to be applied in higher confidence for air quality research and potentially policy decisions.

OMI VCD FNR and NO_2 retrievals display high correlation with surface in situ data trends (see Table 1). However, this satellite demonstrated less capability to replicate trends of surface-level observations of HCHO. The vertical structure of HCHO can be complex which complicates the relationship between VCDs and surface-level values (Souri et al., 2023b); however, OMI has also been shown to have large systematic and random biases in HCHO retrievals which drive the overall errors in OMI-derived VCD FNRs (Johnson et al., 2023; Souri et al., 2023a). However, since decreasing NO_2 emissions/concentrations driven by NO_x emission control strategies is the primary reason for the increasing trends of FNRs at the surface, while HCHO has near-neutral trends, and OMI NO_2 VCDs have much lower errors compared to HCHO (Johnson et al., 2023; Souri et al., 2023a), this study shows that OMI VCD data of indicator species can still replicate surface-level trends of FNRs. Emission control strategies for VOCs have also been shown to have caused regional reductions in the concentrations of these compounds; however, it is challenging to derive and assess the impact of VOC emission control strategies as there are thousands of different VOC compounds all with different chemical reactivity (Pei et al., 2022). Furthermore, a large fraction of VOCs is emitted from biogenic sources which cannot be controlled through changes in human activities (Guenther et al., 1995). In addition to retrieval errors, the coarse spatial resolution of OMI and other spaceborne sensors results in representation errors when compared to point-source surface observations (Souri et al., 2022). This also likely contributes to the challenge of satellite-derived HCHO, NO_2, and FNRs to replicate trends and variability determined from in situ measurements located in city centers.

Besides the southeast US and some small areas of eastern China, OMI HCHO version 3 collection 3 data results in mostly positive trends between 2005-2021. A portion of this positive trend could be due to the OMI instrument drift which has been identified in past studies (e.g., Marais et al., 2012; Zhu et al., 2016, 2017b). Currently, there is an OMI HCHO version 3 collection

4 product in development using the SAO algorithm; however, has yet to be published and therefore could not be applied in this study. A major difference between the collection 3 and 4 data products is how level 1b (L1b) data is produced as described in Kleipool et al. (2022). Furthermore, changes in molecular absorption cross-sections and input parameters for SCD calculations, AMF calculations, and latitudinal bias corrections are applied in collection 4 OMI HCHO data. Preliminary analysis of the differences in OMI VCD HCHO using the collection 3 and 4 data demonstrates changes in the magnitudes and trends of this species (personal communication with the SAO OMI HCHO algorithm team). These differences could have an impact on the analysis of trends in global FNRs such as that conducted in this study. Once the OMI HCHO version 3 collection 4 product becomes available to the public the analysis in this study should be redone with the updated HCHO data. Overall, we don't expect that the results in FNR trends will be impacted much due to observed trends in OMI VCD and surface-level NO_2 being much larger than that in HCHO (see Sect. 3.2).

Due to the inadequacy of our current quantitative understanding of exact threshold FNR values marking the O_3 photochemical regime transitions (e.g., Schroeder et al., 2017), this study avoided explicitly linking OMI FNRs with exact chemical regimes. An accurate diagnosis of surface O_3 sensitivity requires more in-depth analysis of satellite FNRs at a higher spatiotemporal resolution, and accurately relating these FNRs to O_3 regimes by estimating the threshold ratio values applicable to specific regions and time periods. Global CTM simulations (Jin et al., 2017), photochemical box modeling utilizing measurement data from airborne field campaigns (Schroeder et al., 2017; Souri et al., 2020), and observation-based methods linking ratio values with surface O_3 concentrations (Jin et al., 2020; Wang et al., 2021) could lead to the derivation of more accurate regime threshold ratio values. Nevertheless, the OMI-derived VCD FNR values investigated in this study revealed many aspects of O_3 sensitivity to NO_x versus VOCs. In general, OMI-derived summer FNR values indicated radical limited regimes within many cities in the Northern Hemisphere (FNRs < 2) and NO_x-limited regimes over the rural regions around those cities (FNRs > 3). The analysis of multi-year summer mean OMI HCHO and NO_2 values revealed a positive trend in FNRs indicating a transition from radical-limited to NO_x-limited regimes, especially during more recent years. The positive trend in OMI FNRs over most cities are mainly due to decreases in NO_2 resulting from the decrease in anthropogenic NO_x emissions and mixed-variations in biogenic VOC sources. This study evaluated FNR trends for 46 large Northern Hemisphere cities which expands on other recent studies which evaluated O_3 production sensitivity regimes around smaller numbers of cities (e.g., Jin et al., 2017). Due to the majority of highly-populated Northern Hemisphere cities, outside of the Tropics, residing in developed nations, the increasing trend in FNRs due to anthropogenic emissions reductions holds true for the vast majority of the 46 cities studied here.

In the earliest years of studying satellite-derived FNRs it was hoped this data source could potentially be used for policy decisions and developing emission control strategies (Martin et al., 2004). However, more recent studies starting with Duncan et al. (2010) suggested that satellite retrievals may have errors too large for applying FNRs for air quality regulations. Furthermore, satellite data typically has to be temporally averaged to reduce noise in the retrievals which may mask out important O_3 exceedance events and the indicator species characteristics on these days (Schroeder et al., 2017). The recent study by Souri et al. (2023a) compiled a comprehensive error budget for using satellite retrievals to assess surface-level FNRs. This study showed that total relative error in satellite FNRs over large cities tend to be ~50% whereas over rural regions there are much larger errors (>100%). The majority of this error comes from noise in satellite retrievals (40%-90%), especially from HCHO retrievals, and the rest of this error is associated with the ability of indicator species to accurately describe complex O_3 chemistry (~20%), VCD to surface translation (~19%), and spatial representation (~13%). These total relative errors are likely too large to apply satellite FNRs for air quality regulation purposes; however, still provide a useful scientific research product for investigating long-term, and short-term events (e.g., meteorological variations, droughts/floods, wildfires, socioeconomic events, etc.), impacts of emissions on O_3 production sensitivity regimes.

4 Conclusions

This study applied the 17-year data record of OMI satellite sensor's summer mean VCD HCHO, NO$_2$, and FNRs between 2005 and 2021 over the Northern Hemisphere to understand the long-term evolution of O$_3$ photochemical regimes. This expands the global OMI record of VCD FNRs out to 2021 further than previous studies (e.g., Jin et al., 2020). The long-term trends for 46 highly populated cities in the Northern Hemisphere agree with past work which have shown that FNRs are primarily increasing due to reductions in emissions/concentrations of NO$_x$ (Duncan et al., 2010; Jin et al., 2017, 2020). OMI VCD NO$_2$ data are decreasing in most urban regions of the Northern Hemisphere, while HCHO data is near-neutral or slightly increasing, resulting in the increasing FNR trends. The extension of OMI FNR data out to 2021 suggests a continuing trend towards more NO$_x$-limited O$_3$ production sensitivity regimes within and around cities throughout the Northern Hemisphere.

Another unique finding in our study is the extension of OMI FNR data out to 2021 covering the impact of the COVID-19 lockdown of 2020. Out of the 46 selected cities, ~70% of urban regions experienced higher FNRs in 2020 compared to 2019 and ~57% had higher FNRs in 2020 compared to 2021. OMI FNRs were 18%-19% higher in 2020 compared to the year before and after the COVID-lockdown in 2020. We studied summer-mean FNRs in this study; however, COVID-lockdown restrictions were largest in the spring of 2020, thus the full impact of COVID-lockdown restrictions on VCD FNRs was likely larger than that experienced in the summer. A similar percentage of rural areas around the 46 selected cities experience higher FNRs in 2020 compared to 2019 and 2021; however, the increases in FNRs were smaller (13%-16%) compared to urban areas. The OMI data evaluated here suggests that the majority of cities in the Northern Hemisphere, and surrounding rural regions, tended to have O$_3$ production which was more sensitive to NO$_x$ emissions/concentrations in 2020 compared to the year before and after.

Past studies have shown that mid-day FNR VCDs are similar to those observed at the surface (Jin et al., 2017; Souri et al., 2023a). However, during times where HCHO and NO$_2$ vertical profiles in the troposphere are complex, models and satellites may be challenged to accurately assess conversion ratios of VCD FNRs to PBL/surface values (e.g., Souri et al., 2023b). This study shows that on average the long-term trends of OMI VCD FNRs agree well with in observations at the surface in cities distributed around the US, suggesting that this satellite is capable to assess the long-term trends of surface-level O$_3$ production sensitivity regimes. However, the magnitudes of both indicator species calculated with satellite VCDs using scaling factors derived with CTMs and/or in situ observations are highly uncertain. Both OMI VCD and surface in situ data of HCHO, NO$_2$, and FNRs emphasize that the increasing trend in FNRs is driven by reduced emissions/concentrations of NO$_2$ while HCHO has a near-neutral trend. While OMI VCD HCHO trends and variability do not agree well with surface in situ observations; OMI does replicate the strong decreasing trend of NO$_2$ observed at the surface resulting in the agreement between OMI and surface data of FNR trends.

Higher spatiotemporal retrievals from newer low earth orbit (e.g., TROPOMI) and geostationary (e.g., Tropospheric Emissions: Monitoring of Pollution [TEMPO], Geostationary Environment Monitoring Spectrometer [GEMS]) satellite sensors provide more insight into the short-term (daily, diurnal) recent (2017-present) evolution of O$_3$ photochemical regimes. Compared to OMI, TROPOMI was shown to retrieve VCD FNR values with more accuracy and better precision compared to OMI observations primarily due to improvements in HCHO product performance (e.g., Johnson et al., 2023). Johnson et al. (2023) demonstrated that TROPOMI can retrieve spatiotemporal HCHO variability with uncertainties low enough to capture FNR variability on a daily basis, while OMI was not. The current study compared the capability of OMI and TROPOMI to capture inter-city and interannual FNR variability measured by ground-based AQS data (using normalized FNR values) for 7 select US cities. Here we quantitatively showed that TROPOMI was able to reproduce the spatiotemporal variability in observed FNRs more accurately compared to OMI for the reasons mentioned above. Future improvements in satellite HCHO retrievals will allow for more accurate retrievals of FNRs on a daily- to monthly-scale. TEMPO and GEMS provide HCHO and NO$_2$ VCD information at 1- to 3-hour temporal resolution and higher spatial resolution compared to both OMI and TROPOMI which will allow for the

assessment of diurnal FNR variability on a regional scale. This has not yet been possible as TEMPO and GEMS are the first UV/VIS spectrometers on geostationary platforms with spatial resolution high enough to retrieve air quality relevant HCHO and NO_2 VCD data. The new diurnal and high spatial resolution information from these geostationary satellites are expected to greatly improve the understanding of FNRs. As OMI is set to be decommissioned in the coming years, it is critical to merge TROPOMI HCHO and NO_2 VCD data with OMI in order to continue the long-term data set from 2005-present. Furthermore, combining retrieved information from geostationary satellites with once-a-day low earth orbit data will provide a vast wealth of information about global daily to hourly variability in FNRs.

While recent studies have shown that OMI FNR retrieval errors are likely too large to apply in air quality regulation and for deriving emission control strategies to reduce surface-level O_3 concentrations, this long-term satellite product provides a useful scientific research product for investigating atmospheric O_3 chemistry and investigating qualitative impacts of emission changes on O_3 production sensitivity regimes. This is especially true for regions of the globe outside of the US and Europe that have limited long-term surface in situ observation networks able to measure HCHO and NO_2 concentrations. Improvements in HCHO and NO_2 VCD retrieval algorithms and methods to derive VCD to surface/PBL conversion factors for these indicator species would greatly improve the ability to apply OMI and other satellite products to study surface air quality. Data assimilation and inverse models have been combined with satellite retrievals of HCHO and NO_2 data to constrain predictions of NO_x and VOC emissions and resulting O_3 chemistry (e.g., Souri et al., 2020). These satellite data-constrained models can then be used to assess trends and variability in FNRs, indicator species emissions, and O_3 photochemistry regimes. These improvements in satellite retrieval algorithms, CTMs, data assimilation and inverse modeling techniques, along with studies to better define the actual O_3 production sensitivity regime thresholds, will allow for a more confident investigation of long-term air quality and the impacts of NO_x and VOC emission changes on O_3 production sensitivity.

Code and Data Availability. The OMI HCHO L3 data used in this paper is publicly available at https://acdisc.gesdisc.eosdis.nasa.gov/data//Aura_OMI_Level3/OMHCHOd.003/ (last access: 24 October 2021). The OMI NO_2 High Resolution L3 data is also available at a public data repository: https://avdc.gsfc.nasa.gov/pub/data/satellite/Aura/OMI/V03/L3/OMNO2d_HR/OMNO2d_HRD/ (last access: 3 December 2021). The CEDS emission inventory used in this work is also publicly available (https://data.pnnl.gov/group/nodes/dataset/13488) (last access: July 22, 2023). EPA AQS data of HCHO and NO_2 can be downloaded from: https://www.epa.gov/outdoor-air-quality-data/download-daily-data (last access: August 3, 2023).

Supplement. The supplement related to this article is available.

Author Contributions. MJ and SP obtained the funding for this project. MJ, SP, and RK were fundamental in developing the investigation strategy of this study. SJ, SP, SM, S M-H, and YS conducted the analysis which produce the results presented in this manuscript. Finally, MJ and SP were the primary authors which wrote the text of the manuscript.

Competing interests. The authors declare that they have no conflict of interest.

Acknowledgements. Computational resources were provided by the NASA High-End Computing Program through the NASA Advanced Supercomputing Division at NASA Ames Research Center. We acknowledge the United States Environmental

578   Protection Agency for the free availability of in situ data. The views, opinions and findings of this paper are those of the authors

579   and should not be construed as an official NASA or United States Government position, policy, or decision.

580   *Financial support.* The MJ, SP, SM, RK, S M-H, and YS acknowledge funding support from the NASA Earth Science Division's

581   Aura Science Team (NNH19ZDA001N-AURAST) as part of the Upper Atmosphere Research Program (UARP). A part of this

582   material is based upon work supported by the NSF National Center for Atmospheric Research, which is a major facility sponsored

583   by the U.S. National Science Foundation under Cooperative Agreement No. 1852977.

584

References

Acdan, J. J. M., Pierce, R. B., Dickens, A. F., Adelman, Z., and Nergui, T.: Examining TROPOMI formaldehyde to nitrogen dioxide ratios in the Lake Michigan region: implications for ozone exceedances, Atmos. Chem. Phys., 23, 7867–7885, https://doi.org/10.5194/acp-23-7867-2023, 2023.

Anderson, D. C., Nicely, J. M., Wolfe, G. M., Hanisco, T. F., Salawitch, R. J., Canty, T. P., Dickerson, R. R., Apel, E. C., Baidar, S., Bannan, T. J., Blake, N. J., Chen, D., Dix, B., Fernandez, R. P., Hall, S. R., Hornbrook, R. S., Gregory Huey, L., Josse, B., Jöckel, P., Kinnison, D. E., Koenig, T. K., Le Breton, M., Marécal, V., Morgenstern, O., Oman, L. D., Pan, L. L., Percival, C., Plummer, D., Revell, L. E., Rozanov, E., Saiz-Lopez, A., Stenke, A., Sudo, K., Tilmes, S., Ullmann, K., Volkamer, R., Weinheimer, A. J., and Zeng, G.: Formaldehyde in the Tropical Western Pacific: Chemical Sources and Sinks, Convective Transport, and Representation in CAM-Chem and the CCMI Models, J. Geophys. Res.-Atmos., 122, 11201–11226, https://doi.org/10.1002/2016JD026121, 2017.

Ayazpour, Z., Abad, G. G., Nowlan, C. R., Sun, K., Kwon, H. A., Miller, C. C., et al.: Aura Ozone Monitoring Instrument (OMI) Collection 4 Formaldehyde Product, ESS Open Archive, http://dx.doi.org/10.22541/essoar.171804891.19520982/v1, 2024.

Boersma, K. F., Eskes, H. J., Dirksen, R. J., van der A, R. J., Veefkind, J. P., Stammes, P., Huijnen, V., Kleipool, Q. L., Sneep, M., Claas, J., Leitão, J., Richter, A., Zhou, Y., and Brunner, D.: An improved tropospheric NO2 column retrieval algorithm for the Ozone Monitoring Instrument, Atmos. Meas. Tech., 4, 1905–1928, https://doi.org/10.5194/amt-4-1905-2011, 2011.

Boys, B., Martin, R., van Donkelaar, A., MacDonell, R., Hsu, C., Cooper, M., Yantosca, R., Lu, Z., Streets, D. G., Zhang, Q., and Wang, S.: Fifteen-year global time series of satellite-derived fine particulate matter, Environ. Sci. Technol., 48, 11109–11118, 2014.

Bucsela, E. J., Krotkov, N. A., Celarier, E. A., Lamsal, L. N., Swartz, W. H., Bhartia, P. K., Boersma, K. F., Veefkind, J. P., Gleason, J. F., and Pickering, K. E.: A new stratospheric and tropospheric NO2 retrieval algorithm for nadir-viewing satellite instruments: applications to OMI, Atmos. Meas. Tech., 6, 2607–2626, https://doi.org/10.5194/amt-6-2607-2013, 2013.

Burrows, J. P., Weber, M., Buchwitz, M., Rozanov, V., Ladstätter-Weißenmayer, A., Richter, A., DeBeek, R., Hoogen, R., Bramstedt, K., Eichmann, K.-U., Eisingera, M., and Pernerb, D.: The global ozone monitoring experiment (GOME): Mission concept and first scientific results, J. Atmos. Sci., 56, 151–175, 1999.

Camalier, L., Cox, W., and Dolwick, P.: The effects of meteorology on ozone in urban areas and their use in assessing ozone trends, Atmos. Environ., 41, 7127-7137, doi: 10.1016/j.atmosenv.2007.04.061, 2007.

Chance, K. V. and Spurr, R. J. D.: Ring effect studies: Rayleigh scattering, including molecular parameters for rotational Raman scattering, and the Fraunhofer spectrum, Appl. Optics, 36, 5224– 5230, doi:10.1364/AO.36.005224, 1997.

Chance, K.: Analysis of BrO measurements from the Global Ozone Monitoring Experiment, Geophys. Res. Lett., 25, 3335–3338, https://doi.org/10.1029/98GL52359, 1998.

Chang, C. -Y., Faust, E., Hou, X., Lee, P., Kim, H. C., Hedquist, B. C., and Liao, K. -J.: Investigating ambient ozone formation regimes in neighboring cities of shale plays in the northeast United States using photochemical modeling and satellite retrievals, Atmos. Environ., 142, 152–170. doi:10.1016/j.atmosenv.2016.06.058, 2016.

Choi, Y. and Souri, A.: Chemical condition and surface ozone in large cities of Texas during the last decade: observational evidence from OMI, CAMS, and Model Analysis, Remote Sens. Environ., 168, 90–101, https://doi.org/10.1016/j.rse.2015.06.026, 2015.

Choi, Y., Kim, H., Tong, D., and Lee, P.: Summertime weekly cycles of observed and modeled NOx and O3 concentrations as a function of satellite-derived ozone production sensitivity and land use types over the Continental United States, Atmos. Chem. Phys., 12, 6291–6307, doi:10.5194/acp-12-6291-2012, 2012.

Cooper, M. J., Martin, R. V., McLinden, C. A., and Brook, J. R.: Inferring ground-level nitrogen dioxide concentrations at fine spatial resolution applied to the TROPOMI satellite instrument, Environ. Res. Lett., 15, 104013, https://doi.org/10.1088/1748-9326/aba3a5, 2020.

Cooper, M. J., Martin, R. V., Hammer, M. S., Levelt, P. F., Veefkind, P., Lamsal, L. N., Krotkov, N. A., Brook, J. R., and McLinden, C. A.: Global fine-scale changes in ambient NO_2 during COVID-19 lockdowns, Nature, 601, 380–387, 10.1038/s41586-021-04229-0, 2022.

Dave, J. V.: Meaning of successive iteration of the auxiliary equation in the theory of radiative transfer, Astrophys. J., 140, 1292–1303, 1964.

De Smedt, I., Stavrakou, T., Hendrick, F., Danckaert, T., Vlemmix, T., Pinardi, G., Theys, N., Lerot, C., Gielen, C., Vigouroux, C., Hermans, C., Fayt, C., Veefkind, P., Müller, J.-F., and Van Roozendael, M.: Diurnal, seasonal and long-term variations of global formaldehyde columns inferred from combined OMI and GOME-2 observations, Atmos. Chem. Phys., 15, 12519–12545, https://doi.org/10.5194/acp-15-12519-2015, 2015.

De Smedt, I., Theys, N., Yu, H., Danckaert, T., Lerot, C., Compernolle, S., Van Roozendael, M., Richter, A., Hilboll, A., Peters, E., Pedergnana, M., Loyola, D., Beirle, S., Wagner, T., Eskes, H., van Geffen, J., Boersma, K. F., and Veefkind, P.: Algorithm theoretical baseline for formaldehyde retrievals from S5P TROPOMI and from the QA4ECV project, Atmos. Meas. Tech., 11, 2395–2426, https://doi.org/10.5194/amt-11-2395-2018, 2018.

Demuzere, M., He, C., Martilli, A., Zonato, A.: Technical documentation for the hybrid 100-m global land cover dataset with Local Climate Zones for WRF. https://doi.org/10.5281/zenodo.7670791, 2023.

Dobber, M., Kleipool, Q., Dirksen, R., Levelt, P., Jaross, G., Taylor, S., Kelly, T., and Flynn, L.: Validation of ozone monitoring instrument level-1b data products, J. Geophys. Res., 113, D15S06, https://doi.org/10.1029/2007JD008665, 2008.

Duncan, B., Yoshida, Y., Olson, J., Sillman, S., Martin, R., Lamsal, L., Hu, Y., Pickering, K. Retscher, D. Allen, D., and Crawford, J.: Application of OMI observations to a space-based indicator of NOx and VOC controls on surface ozone formation, Atmos. Environ., 44, 2213–2223, https://doi.org/10.1016/j.atmosenv.2010.03.010, 2010.

Fan, C., Li, Z., Li, Y., Dong, J., van der A, R., and de Leeuw, G.: Variability of NO2 concentrations over China and effect on air quality derived from satellite and ground-based observations, Atmos. Chem. Phys., 21, 7723–7748, https://doi.org/10.5194/acp-21-7723-2021, 2021.

GBD 2019 Risk Factor Collaborators: Global burden of 87 risk factors in 204 countries and territories, 1990–2019: a systematic analysis for the Global Burden of Disease Study 2019, The Lancet, 396, 1223–1249, https://doi.org/10.1016/s0140-6736(20)30752-2, 2020.

Geddes, J. A., Martin, R. V., Boys, B. L., and van Donkelaar, A.: Long term trends worldwide in ambient NO_2 concentrations inferred from satellite observations, Environ. Health Perspect., doi:10.1289/ehp.1409567, 2016.

Goldberg, D. L., Anenberg, S. C., Griffin, D., McLinden, C. A., Lu, Z., and Streets, D. G.: Disentangling the Impact of the COVID-19 Lockdowns on Urban NO_2 From Natural Variability, Geophys. Res. Lett., 47, e2020GL089269, https://doi.org/10.1029/2020GL089269, 2020.

González Abad, G., Liu, X., Chance, K., Wang, H., Kurosu, T. P., and Suleiman, R.: Updated Smithsonian Astrophysical Observatory Ozone Monitoring Instrument (SAO OMI) formaldehyde retrieval, Atmos. Meas. Tech., 8, 19–32, doi:10.5194/amt-8-19-2015, 2015.

González Abad, G., Souri, A. H., Bak, J., Chance, K., Flynn, L. E., Krotkov, N. A., Lamsal, L., Li, C., Liu, X., Miller, C. C., Nowlan, C. R., Suleiman, R., and Wang, H.: Five decades observing Earth's atmospheric trace gases using ultraviolet and visible backscatter solar radiation from space, J. Quant. Spectrosc. Ra., 238, 106478, https://doi.org/10.1016/j.jqsrt.2019.04.030, 2019.

Guenther, A., Hewitt, N., Erickson, D., Fall, R., Geron, C., Graedel, T., Harley, P., Klinger, L., Lerdau, M., McKay, W., Pierce, T., Scholes, B., Steinbrecher, R., Tallamraju, R., Taylor, J., and Zimmerman, P.: A global model of natural volatile organic compound emissions, J. Geophys. Res., 100, 8873–8892, 1995.

He, G., Pan, Y. and Tanaka, T.: The short-term impacts of COVID-19 lockdown on urban air pollution in China, Nature Sustainability, 3(12), 1005–1011, https://doi.org/10.1038/s41893-020-0581-y, 2020.

Hilboll, A., Richter, A., and Burrows, J. P.: Long-term changes of tropospheric NO2 over megacities derived from multiple satellite instruments, Atmos. Chem. Phys., 13, 4145–4169, https://doi.org/10.5194/acp-13-4145-2013, 2013.

Itahashi, S., Irie, H., Shimadera, H., and Chatani, S.: Fifteen-Year Trends (2005–2019) in the Satellite-Derived Ozone-Sensitive Regime in East Asia: A Gradual Shift from VOC-Sensitive to NOx-Sensitive, Remote Sens., 14, 4512, https://doi.org/10.3390/rs14184512, 2022.

Jacob, D. J., Horowitz, L. W., Munger, J. W., Heikes, B. G., Dickerson, R. R., Artz, R. S., and Keene, W. C.: Seasonal transition from NOx- to hydrocarbon-limited conditions for ozone production over the eastern United States in September, J. Geophys. Res.-Atmo., 100, 9315–9324, https://doi.org/10.1029/94JD03125, 1995.

Jin, X., and Holloway, T.: Spatial and temporal variability of ozone sensitivity over China observed from the Ozone Monitoring Instrument, J. Geophys. Res. Atmos., 120, 7229–7246, doi:10.1002/2015JD023250, 2015.

Jin, X., Fiore, A. M., Murray, L. T., Valin, L. C., Lamsal, L. N., Duncan, B., Boersma, K. F., De Smedt, I., Abad, G. G., Chance, K., and Tonnesen, G. S.: Evaluating a Space-Based Indicator of Surface Ozone-NOx-VOC Sensitivity Over Midlatitude Source Regions and Application to Decadal Trends, J. Geophys. Res.-Atmos., 122, 10439–10461, https://doi.org/10.1002/2017JD026720, 2017.

Jin, X., Fiore, A. M., and Geigert, M.: Using satellite observed formaldehyde (HCHO) and nitrogen dioxide (NO2) as an indicator of ozone sensitivity in a SIP, HAQAST Tech. Guid. Doc. No. 1, doi:10.7916/D8M34C7V, 2018.

Jin, X., Fiore, A., Boersma, K. F., De Smedt, I., and Valin, L.: Inferring Changes in Summertime Surface Ozone–NOx–VOC Chemistry over U.S. Urban Areas from Two Decades of Satellite and Ground-Based Observations, Environ. Sci. Technol., 54, 6518–6529, https://doi.org/10.1021/acs.est.9b07785, 2020.

Johnson, M. S., Souri, A. H., Philip, S., Kumar, R., Naeger, A., Geddes, J., Judd, L., Janz, S., Chong, H., and Sullivan, J.: Satellite remote-sensing capability to assess tropospheric-column ratios of formaldehyde and nitrogen dioxide: case study during the Long Island Sound Tropospheric Ozone Study 2018 (LISTOS 2018) field campaign, Atmos. Meas. Tech., 16, 2431–2454, https://doi.org/10.5194/amt-16-2431-2023, 2023.

Kharol, S. K., Martin, R. V., Philip, S., Boys, B., Lamsal, L. N., Jerrett, M., Brauer, M., Crouse, D. L., McLinden, C., and Burnett, R. T.: Assessment of the magnitude and recent trends in satellite-derived ground-level nitrogen dioxide over North America, Atmos. Environ., 118, 236–245, https://doi.org/10.1016/j.atmosenv.2015.08.011, 2015.

697   Kleinman, L. I.: Low and high NOx tropospheric photochemistry, J. Geophys. Res., 99, 16831–16838, 1994.

698   Kleinman, L. I., Daum, P. H., Lee, Y. N., Nunnermacker, L. J., Springston, S. R., Weinstein-Lloyd, J., and Rudolph, J.: A
699   comparative study of ozone production in five US metropolitan areas, J. Geophys. Res.-Atmos., 110, D02301,
700   doi:10.1029/2004JD005096, 2005.

701   Kleipool, Q., Rozemeijer, N., van Hoek, M., Leloux, J., Loots, E., Ludewig, A., van der Plas, E., Adrichem, D., Harel, R., Spronk,
702   S., ter Linden, M., Jaross, G., Haffner, D., Veefkind, P., and Levelt, P. F.: Ozone Monitoring Instrument (OMI) collection 4:
703   establishing a 17-year-long series of detrended level-1b data, Atmos. Meas. Tech., 15, 3527–3553,
704   https://doi.org/10.5194/amt-15-3527-2022, 2022.

705   Koplitz, S., Simon, H., Henderson, B., Liljegren, J., Tonnesen, G., Whitehill, A., and Wells, B.: Changes in Ozone Chemical
706   Sensitivity in the United States from 2007 to 2016, ACS Environ. Au, 2, 206–222,
707   https://doi.org/10.1021/ACSENVIRONAU.1C00029, 2021.

708   Krotkov, N. A., McLinden, C. A., Li, C., Lamsal, L. N., Celarier, E. A., Marchenko, S. V., Swartz, W. H., Bucsela, E. J., Joiner,
709   J., Duncan, B. N., Boersma, K. F., Veefkind, J. P., Levelt, P. F., Fioletov, V. E., Dickerson, R. R., He, H., Lu, Z., and Streets,
710   D. G.: Aura OMI observations of regional SO2 and NO2 pollution changes from 2005 to 2015, Atmos. Chem. Phys., 16,
711   4605–4629, https://doi.org/10.5194/acp-16-4605-2016, 2016.

712   Krotkov, N. A., Lamsal, L. N., Celarier, E. A., Swartz, W. H., Marchenko, S. V., Bucsela, E. J., Chan, K. L., Wenig, M., and Zara,
713   M.: The version 3 OMI NO2 standard product, Atmos. Meas. Tech., 10, 3133–3149, https://doi.org/10.5194/amt-10-3133-
714   2017, 2017.

715   Lamsal, L. N., Martin, R. V., Steinbacher, M., Celarier, E. A., Bucsela, E., Dunlea, E. J., and Pinto, J.: Ground level nitrogen
716   dioxide concentrations inferred from the satellite-borne Ozone Monitoring Instrument, J. Geophys. Res., 113, D16308,
717   https://doi.org/10.1029/2007JD009235, 2008.

718   Lamsal, L. N., Martin, R. V., van Donkelaar, A., Celarier, E. A., Bucsela, E. J., Boersma, K. F., Dirksen, R., Luo, C., and Wang,
719   Y.: Indirect validation of tropospheric nitrogen dioxide retrieved from the OMI satellite instrument: Insight into the seasonal
720   variation of nitrogen oxides at northern midlatitudes, J. Geophys. Res., 115, D05302, https://doi.org/10.1029/2009JD013351,
721   2010.

722   Lamsal, L. N., Duncan, B. N., Yoshida, Y., Krotkov, N. A., Pickering, K. E., Streets, D. G., and Lu, Z.: U.S. NO2 trends (2005–
723   2013): EPA Air Quality System (AQS) data versus improved observations from the Ozone Monitoring Instrument (OMI),
724   Atmos. Environ., 110, 130–143, doi:10.1016/j.atmosenv.2015.03.055, 2015.

725   Levelt, P. F., Hilsenrath, E., Leppelmeier, G. W., Oord, G. H. J. Van Den, Bhartia, P. K., Tamminen, J., De Haan, J. F., and
726   Veefkind, J. P.: Science Objectives of the Ozone Monitoring Instrument, IEEE T. Geosci. Remote Sens., 44, 1199–1208,
727   2006.

728   Levelt, P. F., Joiner, J., Tamminen, J., Veefkind, J. P., Bhartia, P. K., Stein Zweers, D. C., Duncan, B. N., Streets, D. G., Eskes,
729   H., van der A, R., McLinden, C., Fioletov, V., Carn, S., de Laat, J., DeLand, M., Marchenko, S., McPeters, R., Ziemke, J., Fu,
730   D., Liu, X., Pickering, K., Apituley, A., González Abad, G., Arola, A., Boersma, F., Chan Miller, C., Chance, K., de Graaf,
731   M., Hakkarainen, J., Hassinen, S., Ialongo, I., Kleipool, Q., Krotkov, N., Li, C., Lamsal, L., Newman, P., Nowlan, C.,
732   Suleiman, R., Tilstra, L. G., Torres, O., Wang, H., and Wargan, K.: The Ozone Monitoring Instrument: overview of 14 years
733   in space, Atmos. Chem. Phys., 18, 5699–5745, https://doi.org/10.5194/acp-18-5699-2018, 2018.

Li, Y., Lau, A. K. H., Fung, J. C. H., Zheng, J. Y., Zhong, L. J., and Louie, P. K. K.: Ozone source apportionment (OSAT) to differentiate local regional and super-regional source contributions in the Pearl River Delta region, China, J. Geophys. Res.-Atmos., 117, 1–18, https://doi.org/10.1029/2011JD017340, 2012.

Mahajan, A. S., De Smedt, I., Biswas, M. S., Ghude, S., Fadnavis, S., Roy, C., and van Roozendael, M.: Inter-annual variations in satellite observations of nitrogen dioxide and formaldehyde over India, Atmos. Environ., 116, 194–201, https://doi.org/10.1016/j.atmosenv.2015.06.004, 2015.

Marais, E. A., Jacob, D. J., Kurosu, T. P., Chance, K., Murphy, J. G., Reeves, C., Mills, G., Casadio, S., Millet, D. B., Barkley, M. P., Paulot, F., and Mao, J.: Isoprene emissions in Africa inferred from OMI observations of formaldehyde columns, Atmos. Chem. Phys., 12, 6219–6235, https://doi.org/10.5194/acp-12-6219-2012, 2012.

Marchenko, S., Krotkov, N., Lamsal, L., Celarier, E., Swartz, W., and Bucsela, E.: Revising the slant column density retrieval of nitrogen dioxide observed by the Ozone Monitoring Instrument, J. Geophys. Res., 120, 5670–5692, https://doi.org/10.1002/2014JD022913, 2015.

Martin, R. V., Fiore, A. M., and Van Donkelaar, A.: Space-based diagnosis of surface ozone sensitivity to anthropogenic emissions, Geophys. Res. Lett., 31, L06120. doi:10.1029/2004GL019416, 2004.

McDuffie, E. E., Smith, S. J., O'Rourke, P., Tibrewal, K., Venkataraman, C., Marais, E. A., Zheng, B., Crippa, M., Brauer, M., and Martin, R. V.: A global anthropogenic emission inventory of atmospheric pollutants from sector- and fuel-specific sources (1970–2017): an application of the Community Emissions Data System (CEDS), Earth Syst. Sci. Data, 12, 3413–3442, https://doi.org/10.5194/essd-12-3413-2020, 2020.

Milford, J. B., Gao, D. F., Sillman, S., Blossey, P., and Russell, A. G.: Total reactive nitraogen (NOy) as an indicator of the sensitivity of ozone to reductions in hydrocarbon and NOx emissions, J. Geophys. Res.-Atmos., 99, 3533–3542, https://doi.org/10.1029/93jd03224, 1994.

Millet, D. B., Jacob, D. J., Boersma, K. F., Fu, T.-M., Kurosu, T. P., Chance, K., Heald, C. L., and Guenther, A.: Spatial distribution of isoprene emissions from North America derived from formaldehyde column measurements by the OMI satellite sensor, J. Geophys. Res., 113, D02307, https://doi.org/10.1029/2007JD008950, 2008.

Monks, P. S., Archibald, A. T., Colette, A., Cooper, O., Coyle, M., Derwent, R., Fowler, D., Granier, C., Law, K. S., Mills, G. E., Stevenson, D. S., Tarasova, O., Thouret, V., von Schneidemesser, E., Sommariva, R., Wild, O., and Williams, M. L.: Tropospheric ozone and its precursors from the urban to the global scale from air quality to short-lived climate forcer, Atmos. Chem. Phys., 15, 8889–8973, https://doi.org/10.5194/acp-15-8889-2015, 2015.

Nussbaumer, C. M., Pozzer, A., Tadic, I., Röder, L., Obersteiner, F., Harder, H., Lelieveld, J., and Fischer, H.: Tropospheric ozone production and chemical regime analysis during the COVID-19 lockdown over Europe, Atmos. Chem. Phys., 22, 6151–6165, https://doi.org/10.5194/acp-22-6151-2022, 2022.

Palmer, P. I., Jacob, D. J., Chance, K., Martin, R. V., Spurr, R. J. D., Kurosu, T. P., Bey, I., Yantosca, R., Fiore, A., and Li, Q.: Air mass factor formulation for spectroscopic measurements from satellites: Application to formaldehyde retrievals from the Global Ozone Monitoring Experiment, J. Geophys. Res.-Atmos., 106, 14539–14550, https://doi.org/10.1029/2000JD900772, 2001.

Pei, C. L., Yang, W. Q., Zhang, Y. L., Song, W., Xiao, S. X., Wang, J., Zhang, J. P., Zhang, T., Chen, D. H., Wang, Y. J., Chen, Y. N., and Wang, X. M.: Decrease in ambient volatile organic compounds during the COVID-19 lockdown period in the Pearl River Delta region, South China, Sci. Total Environ., 823, 153720, https://doi.org/10.1016/j.scitotenv.2022.153720, 2022.

772 Philip, S., Martin, R. V., van Donkelaar, A., Lo, J. W., Wang, Y., Chen, D., Zhang, L., Kasibhatla, P. S., Wang, S. W., Zhang, Q.,
773   Lu, Z., Streets, D. G., Bittman, S., and Macdonald, D. J.: Global chemical composition of ambient fine particulate matter for
774   exposure assessment, Environ. Sci. Technol., 48, 13060-13068, doi:10.1021/es502965b, 2014.

775 Schenkeveld, V. M. E., Jaross, G., Marchenko, S., Haffner, D., Kleipool, Q. L., Rozemeijer, N. C., Veefkind, J. P., and Levelt, P.
776   F.: In-flight performance of the Ozone Monitoring Instrument, Atmos. Meas. Tech., 10, 1957–1986,
777   https://doi.org/10.5194/amt-10-1957-2017, 2017.

778 Schoeberl, M. R., Douglass, A. R., Hilsenrath, E., Bhartia, P. K., Beer, R., Waters, J. W., Gunson, M. R., Froidevaux, L., Gille, J.
779   C., Barnett, J. J., Levelt, P. F., and DeCola, P.: Overview of the EOS aura mission, IEEE T. Geosci. Remote Sens., 44, 1066–
780   1072, doi:10.1109/TGRS.2005.861950, 2006.

781 Schroeder, J. R., Crawford, J. H., Fried, A., Walega, J., Weinheimer, A., Wisthaler, A., Müller, M., Mikoviny, T., Chen, G., Shook,
782   M., Blake, D. R., and Tonnesen, G. S.: New insights into the column CH_2ONO_2 ratio as an indicator of near-surface ozone
783   sensitivity, J. Geophys. Res.-Atmos., 122, 8885–8907, https://doi.org/10.1002/2017JD026781, 2017.

784 Seinfeld, J. H. and Pandis, S. N.: Atmospheric Chemistry and Physics: From Air Pollution to Climate Change, John Wiley and
785   Sons, Hoboken, ISBN: 978-1-118-94740-1, 2016.

786 Shen, L., Jacob, D. J., Liu, X., Huang, G., Li, K., Liao, H., and Wang, T.: An evaluation of the ability of the Ozone Monitoring
787   Instrument (OMI) to observe boundary layer ozone pollution across China: application to 2005–2017 ozone trends, Atmos.
788   Chem. Phys., 19, 6551–6560, https://doi.org/10.5194/acp-19-6551-2019, 2019.

789 Sillman, S.: The use of NOy, H2O2, and HNO3 as indicators for O3-NOx-hydrocarbon sensitivity in urban locations, J. Geophys.
790   Res. Atmos., 100, 14175-14188, doi:10.1029/94JD02953, 1995.

791 Sillman, S.: The relation between ozone, NOx, and hydrocarbons in urban and polluted rural environments, Atmos. Environ., 33,
792   1821–1845, 1999.

793 Sillman, S., Logan, J. A., and Wofsy, S. C.: The sensitivity of ozone to nitrogen oxides and hydrocarbons in regional ozone
794   episodes, J. Geophys. Res., 95, 1837-1851, doi: 10.1029/JD095iD02p01837, 1990.

795 Souri, A. H., Choi, Y., Jeon, W., Woo, J. -H., Zhang, Q., and Kurokawa J.-i.: Remote sensing evidence of decadal changes in
796   major tropospheric ozone precursors over East Asia, J. Geophys. Res. Atmos., 122, 2474-2492, doi:10.1002/2016JD025663,
797   2017.

798 Souri, A. H., Nowlan, C. R., Wolfe, G. M., Lamsal, L. N., Chan Miller, C. E., Abad, G. G., Janz, S. J., Fried, A., Blake, D. R.,
799   Weinheimer, A. J., Diskin, G. S., Liu, X., and Chance, K.: Revisiting the effectiveness of HCHO/NO2 ratios for inferring
800   ozone sensitivity to its precursors using high resolution airborne remote sensing observations in a high ozone episode during
801   the KORUS-AQ campaign, Atmos. Environ., 224, 117341, https://doi.org/10.1016/j.atmosenv.2020.117341, 2020.

802 Souri, A. H., Chance, K., Sun, K., Liu, X., and Johnson, M. S.: Dealing with spatial heterogeneity in pointwise-to-gridded- data
803   comparisons, Atmos. Meas. Tech., 15, 41–59, https://doi.org/10.5194/amt-15-41-2022, 2022.

804 Souri, A. H., Johnson, M. S., Wolfe, G. M., Crawford, J. H., Fried, A., Wisthaler, A., Brune, W. H., Blake, D. R., Weinheimer, A.
805   J., Verhoelst, T., Compernolle, S., Pinardi, G., Vigouroux, C., Langerock, B., Choi, S., Lamsal, L., Zhu, L., Sun, S., Cohen,
806   R. C., Min, K.-E., Cho, C., Philip, S., Liu, X., and Chance, K.: Characterization of errors in satellite-based HCHO ⁄ NO2
807   tropospheric column ratios with respect to chemistry, column-to-PBL translation, spatial representation, and retrieval
808   uncertainties, Atmos. Chem. Phys., 23, 1963–1986, https://doi.org/10.5194/acp-23-1963-2023, 2023a.

Souri, A. H., Kumar, R., Chong H., Golbazi, M., Knowland, K. E., Geddes, J., and Johnson, M. S.: Decoupling in the vertical shape of HCHO during a sea breeze event: The effect on trace gas satellite retrievals and column-to-surface translation, Atmospheric Environment, 309, https://doi.org/10.1016/j.atmosenv.2023.119929, 2023b.

Spurr, R. J. D.: VLIDORT: a linearized pseudo-spherical vector discrete ordinate radiative transfer code for forward model and retrieval studies in multilayer multiple scattering media, J. Quant. Spectrosc. Rad. Trans., 102, 316–421, https://doi.org/10.1016/j.jqsrt.2006.05.005, 2006.

Stewart, I. D. and Oke, T. R.: Local Climate Zones for Urban Temperature Studies, B. Am. Meteorol. Soc., 93, 1879–1900, https://doi.org/10.1175/BAMS-D-11-00019.1, 2012.

Tai, A., Martin, M., and Heald, C.: Threat to future global food security from climate change and ozone air pollution, Nature Clim Change, 4, 817–821, https://doi.org/10.1038/nclimate2317, 2014.

Tao, M., Fiore, A. M., Jin, X., Schiferl, L. D., Commane, R., Judd, L. M., Janz, S., Sullivan, J. T., Miller, P. J., Karambelas, A., Davis, S., Tzortziou, M., Valin, L., Whitehill, A., Civerolo, K., and Tian, Y.: Investigating changes in ozone formation chemistry during summertime pollution vents over the northeastern United States, Environ. Sci. Technol., 56, 15312–15327, https://doi.org/10.1021/acs.est.2c02972, 2022.

Tonnesen, G. S., and Dennis, R. L.: Analysis of radical propagation efficiency to assess O3 sensitivity to hydrocarbons and NOx: 2. Long-lived species as indicators of O3 concentration sensitivity, J. Geophys. Res. Atmos., 105, 9227–9241. Doi:10.1029/1999JD900372, 2000.

US Environmental Protection Agency (US EPA): Air Quality Criteria for Ozone and Related Photochemical Oxidants (2006 Final), U.S. Environmental Protection Agency, Washington, DC, EPA/600/R-05/004aF-cF, 2006.

Wang, W., van der A, R., Ding, J., van Weele, M., and Cheng, T.: Spatial and temporal changes of the ozone sensitivity in China based on satellite and ground-based observations, Atmos. Chem. Phys., 21, 7253–7269, https://doi.org/10.5194/acp-21-7253-2021, 2021.

Witte, J., Duncan, B., Douglass, A., Kurosu, T., Chance, K., and Retscher, C.: The unique OMI HCHO NO2 feature during the 2008 Beijing Olympics: Implications for ozone production sensitivity, Journal: Atmospheric Environment, 45, 3103–3111, https://doi.org/10.1016/j.atmosenv.2011.03.015, 2011.

Wu, S., Duncan, B. N., Jacob, D. J., Fiore, A. M. and Wild, O.: Chemical nonlinearities in relating intercontinental ozone pollution to anthropogenic emissions, Geophys. Res. Lett., 36, L05806, doi:10.1029/2008GL036607, 2009.

Zhang, L., Jacob, D. J., Kopacz, M., Henze, D. K., Singh, K., and Jaffe, D. A.: Intercontinental source attribution of ozone pollution at western U.S. sites using an adjoint method, Geophys. Res. Lett., 36, L11810, https://doi.org/10.1029/2009GL037950, 2009.

Zhu, L., Jacob, D. J., Mickley, L. J., Marais, E. A., Cohan, D. S., Yoshida, Y., Duncan, B. N., González Abad, G., and Chance, K. V.: Anthropogenic emissions of highly reactive volatile organic compounds in eastern Texas inferred from oversampling of satellite (OMI) measurements of HCHO columns, Environ. Res. Lett., 9, 114004, https://doi.org/10.1088/1748-9326/9/11/114004, 2014.

Zhu, L., Jacob, D. J., Kim, P. S., Fisher, J. A., Yu, K., Travis, K. R., Mickley, L. J., Yantosca, R. M., Sulprizio, M. P., De Smedt, I., González Abad, G., Chance, K., Li, C., Ferrare, R., Fried, A., Hair, J. W., Hanisco, T. F., Richter, D., Jo Scarino, A., Walega, J., Weibring, P., and Wolfe, G. M.: Observing atmospheric formaldehyde (HCHO) from space: validation and intercomparison of six retrievals from four satellites (OMI, GOME2A, GOME2B, OMPS) with SEAC4RS aircraft

846   observations over the southeast US, Atmos. Chem. Phys., 16, 13477–13490, https://doi.org/10.5194/acp-16-13477-2016,

847   2016.

848 Zhu, L., Jacob, D. J., Keutsch, F. N., Mickley, L. J., Scheffe, R., Strum, M., González Abad, G., Chance, K., Yang, K.,

849   Rappenglück, B., Millet, D. B., and Baasandorj, M.: Formaldehyde (HCHO) as a Hazardous Air Pollutant: Mapping surface

850   air concentrations from satellite and inferring cancer risks in the United States, Environ. Sci. Technol., 51, 5650–5657,

851   https://doi.org/10.1021/acs.est.7b01356, 2017a.

852 Zhu, L., Mickley, L. J., Jacob, D. J., Marais, E. A., Sheng, J., Hu, L., González Abad, G., and Chance, K.: Long-term (2005–2014)

853   trends in formaldehyde (HCHO) columns across North America as seen by the OMI satellite instrument: Evidence of changing

854   emissions of volatile organic compounds, Geophys. Res. Lett., 44, 7079–7086, https://doi.org/10.1002/2017GL073859,

855   2017b.

856 Zhu, L., González Abad, G., Nowlan, C. R., Chan Miller, C., Chance, K., Apel, E. C., DiGangi, J. P., Fried, A., Hanisco, T. F.,

857   Hornbrook, R. S., Hu, L., Kaiser, J., Keutsch, F. N., Permar, W., St. Clair, J. M., and Wolfe, G. M.: Validation of satellite

858   formaldehyde (HCHO) retrievals using observations from 12 aircraft campaigns, Atmos. Chem. Phys., 20, 12329–12345,

859   https://doi.org/10.5194/acp-20-12329-2020, 2020.

860

861 **Tables**

862

863 **Table 1. Statistics of the correlation of OMI and AQS ("Obs.") normalized trends for HCHO, NO$_2$, and FNRs**
864 **for major cities in the US and the average of all cities in the US (USA urban areas) between 2005-2019. Slopes**
865 **of the trends for each species (units of yr^{-1}) are also provided. The values in italic font are linear regression**
866 **slopes which are statistically significant at a 95% confidence level (p≤0.05).**

Cities	Corr. HCHO	Slope HCHO Obs.	Slope HCHO OMI	Corr. NO$_2$	Slope NO$_2$ Obs.	Slope NO$_2$ OMI	Corr. FNR	Slope FNR Obs.	Slope FNR OMI
New York	0.01	*0.10*	0.05	0.91	*-0.21*	*-0.20*	0.78	*0.20*	*0.20*
Los Angeles	-0.01	-0.14	0.14	0.98	*-0.21*	*-0.22*	0.84	*0.17*	*0.22*
Chicago	NaN	NaN	0.07	0.91	*-0.22*	*-0.21*	NaN	NaN	*0.18*
Washington DC	0.38	*0.11*	0.05	0.89	*-0.19*	*-0.20*	0.77	*0.18*	*0.21*
Pittsburgh	0.51	0.06	0.10	0.64	*-0.21*	*-0.16*	0.55	*0.22*	*0.16*
Atlanta	NaN	NaN	-0.07	0.33	-0.01	*-0.17*	NaN	NaN	*0.18*
Houston	0.40	*-0.18*	-0.06	0.79	*-0.17*	*-0.17*	-0.27	*-0.12*	*0.13*
USA urban areas	0.24	-0.05	*0.15*	0.98	*-0.21*	*-0.20*	0.91	*0.21*	*0.21*

867 Correlation values are the correlation coefficient (R).
868 NaN values indicate cities where particular species data is not available for all years between 2005-2019.
869

870 **Figures**
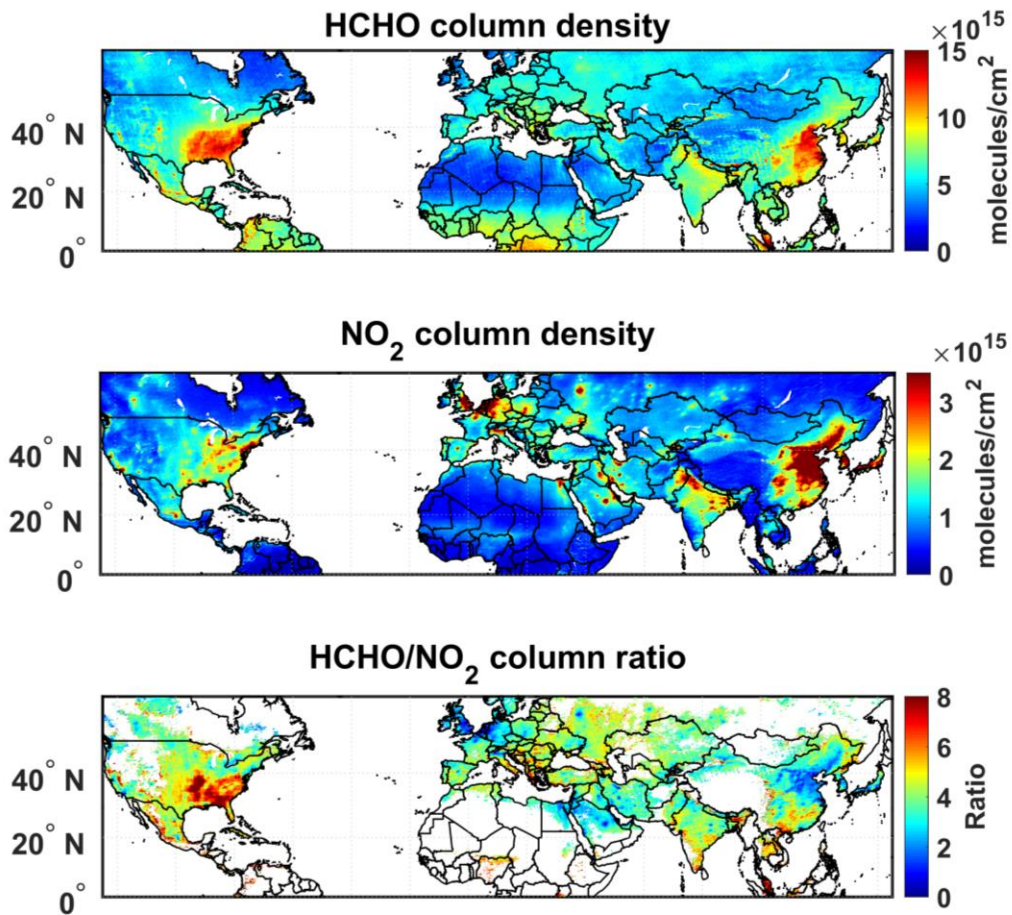
871
872 **Figure 1: OMI-derived multi-year (2005-2021) summer mean (June-August) HCHO VCDs (top row), NO₂ VCDs (middle**
873 **row), and resulting VCD FNRs at $0.1° \times 0.1°$ latitude × longitude grid cells. Values of FNRs are displayed only for polluted**
874 **regions (NO₂ VCD $> 1.2 \times 10^{15}$ molecule cm^{-2}). The white color indicates data gaps or oceanic grid cells.**

875
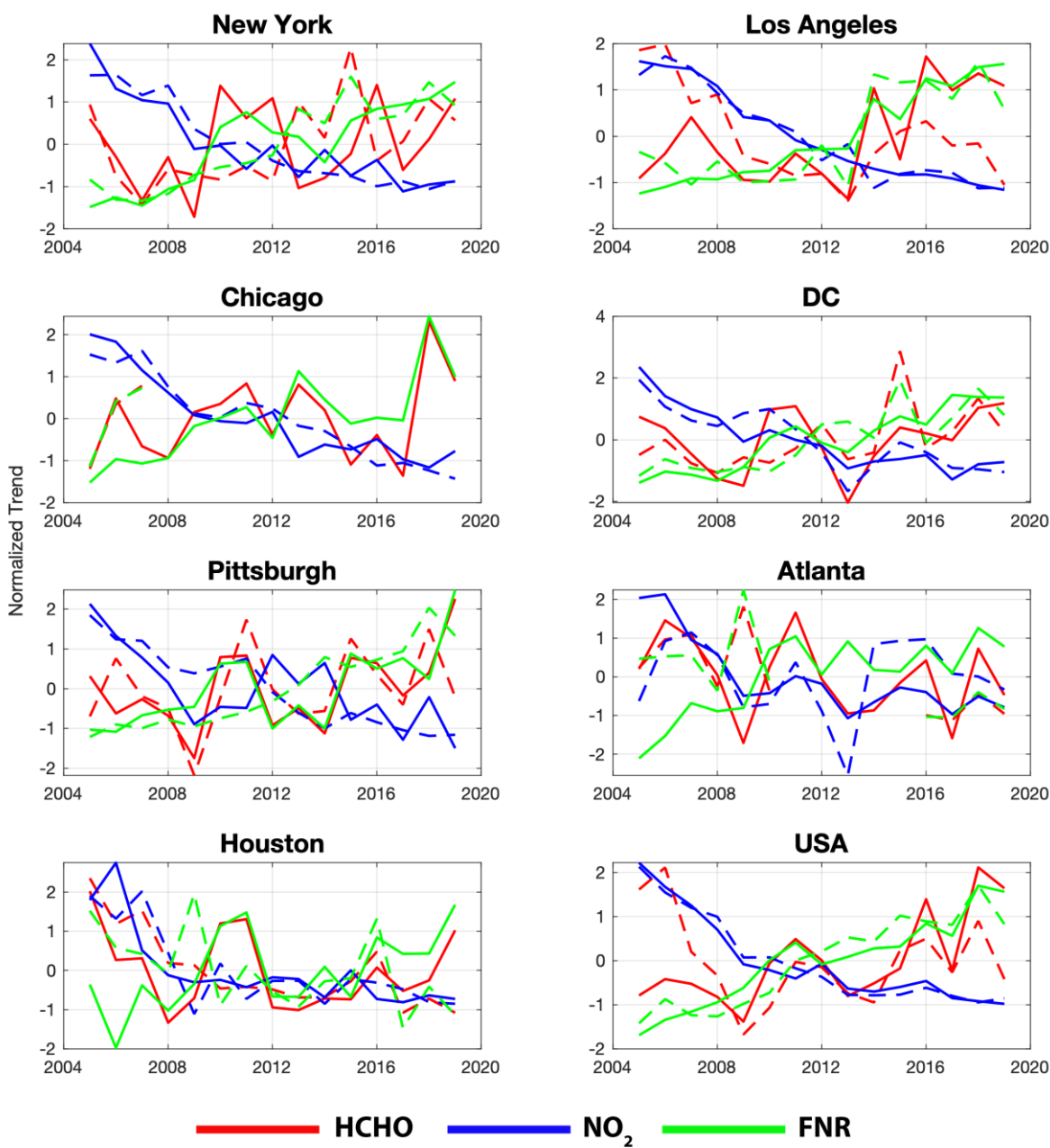
Figure 2: Normalized time series (values from 2005 to 2019 normalized to 2005-2019 mean) of summer mean OMI HCHO and NO₂ VCDs and column FNRs (solid lines). The same information is shown for surface concentrations from the EPA-AQS in situ observations (dashed lines) over select cities and over all urban monitoring sites in the United States (bottom right panel).

882
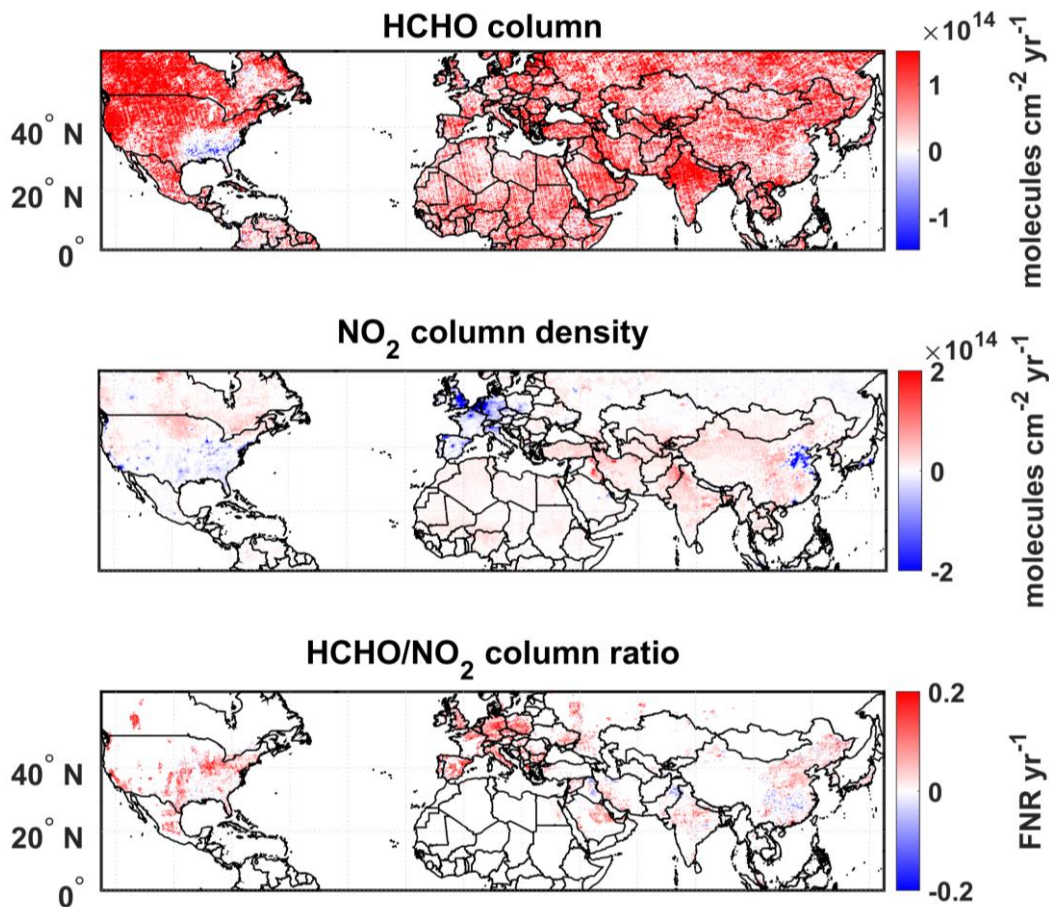
Figure 3: OMI-derived trends in summer mean (June-August) time series of HCHO (top row) and NO_2 (middle row) VCDs (units in molecule cm^{-2} yr^{-1}), and corresponding FNR values (bottom row; unitless yr^{-1}) at $0.1° \times 0.1°$ latitude $\times$ longitude grid cells between 2005 and 2021. Values in the bottom row are displayed only for polluted regions (OMI NO_2 VCD > 1.2 $\times 10^{15}$ molecule cm^{-2}). The white color indicates data gaps or oceanic grid cells. All trend values that are displayed are at an 85% confidence level (p $\leq$ 0.15) for better visualization of spatial trend variability. Figure S1 shows the trend values at 99% confidence level and for all grid cells.

889

890
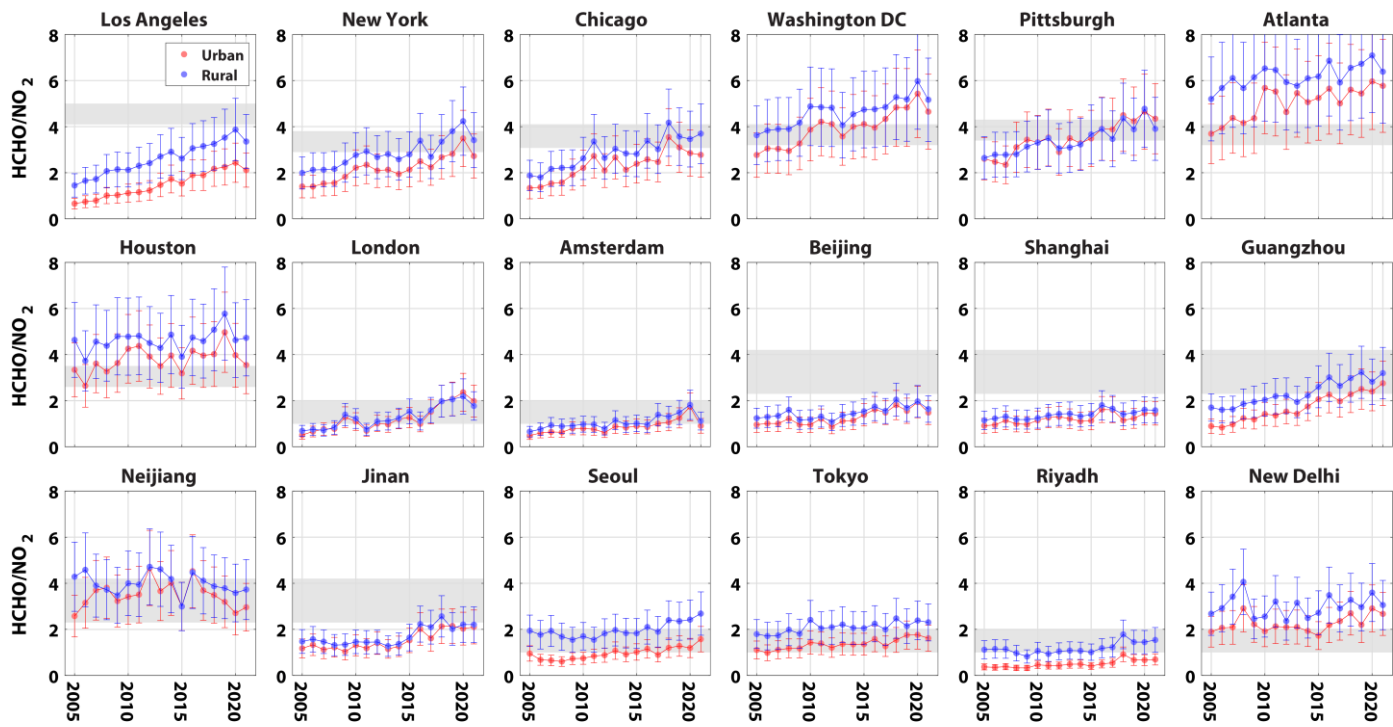
Figure 4: Time series of OMI-derived summer mean (June-August) FNR VCD values for 18 selected cities across the North Hemisphere from 2005 to 2021. The different colors illustrate mean FNR values for urban (red) and rural areas around each city (blue). Grey shaded areas represent the transition zone of ozone production sensitivity regime threshold values as suggested by Jin et al. (2020) (cities in United States: Los Angeles, New York, Chicago, Washington DC, Pittsburgh, Atlanta and Houston), Wang et al. (2021) (cities in China: Beijing, Shanghai, Guangzhou, Neijiang and Jinan), and Duncan et al. (2010) (other cities). For interpretation, FNR values that are less than the transition zone have O_3 production which is VOC-limited and FNR values larger than the transition zone have O_3 production which is NO_x-limited.
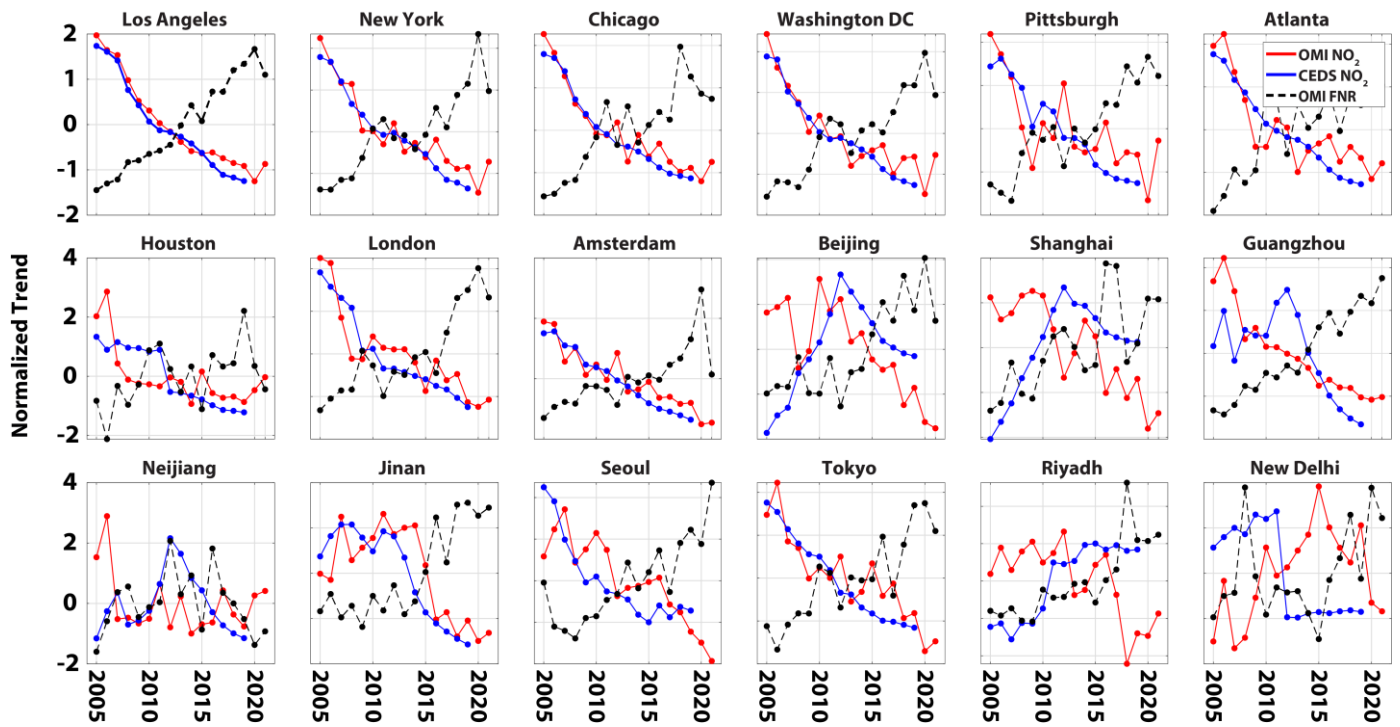
Figure 5: Time series of normalized OMI-derived summer mean (June-August) VCD NO₂ and FNR trend values and corresponding trends in anthropogenic emission of NOₓ from the CEDS bottom-up inventory over the selected 18 cities across the Northern Hemisphere from 2005 to 2021. CEDS emissions data is only displayed until 2019 due to this being the most recent year of availability.

905

906
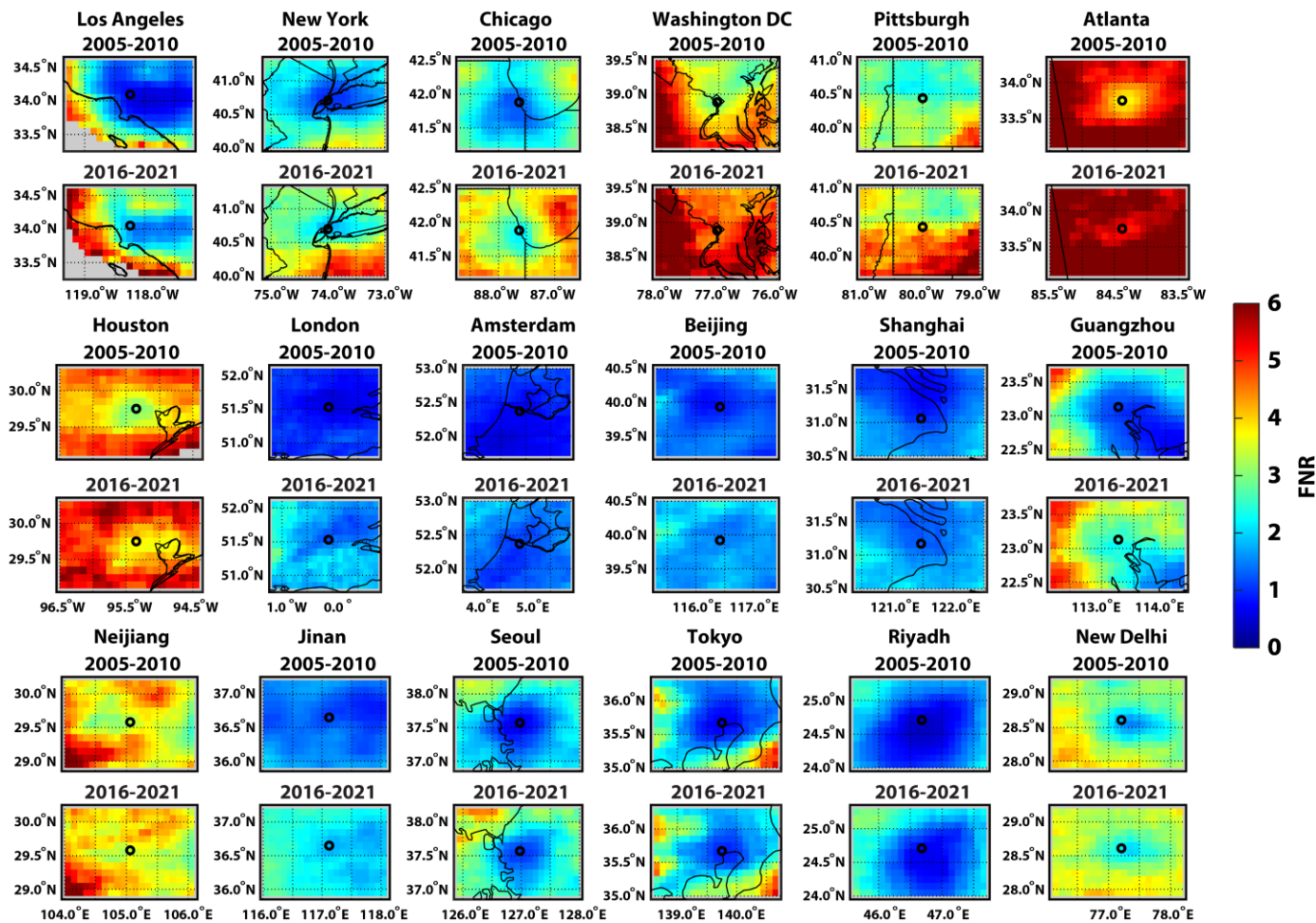
Figure 6: OMI-derived summer mean (June-August) FNR VCD values for 18 selected cities across the Northern Hemisphere during 2005-2010 and 2016-2021. The black circle represents each city center. CGLC-MODIS-LCZ urban grids for each city are displayed in Fig. S10. Grey color indicates data gaps or oceanic grid cells.
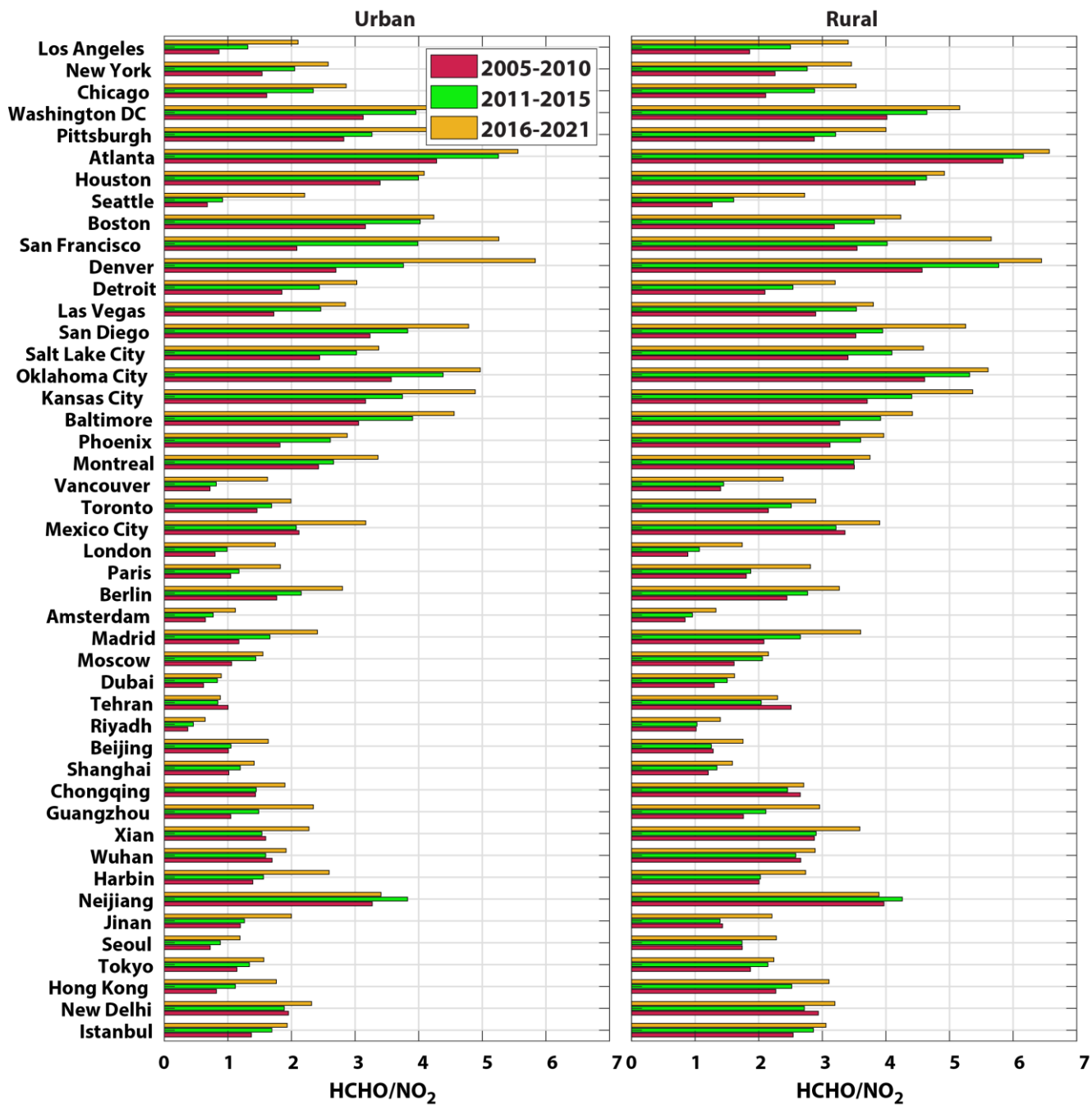
Figure 7: OMI-derived summer-mean (June-August) FNR VCD values for a select 46 cities across the Northern Hemisphere during 2005-2010 (blue), 2011-2015 (red) and 2016-2021 (orange). Each column represents mean ratio values for urban city (left column) and the surrounding rural areas (right column).
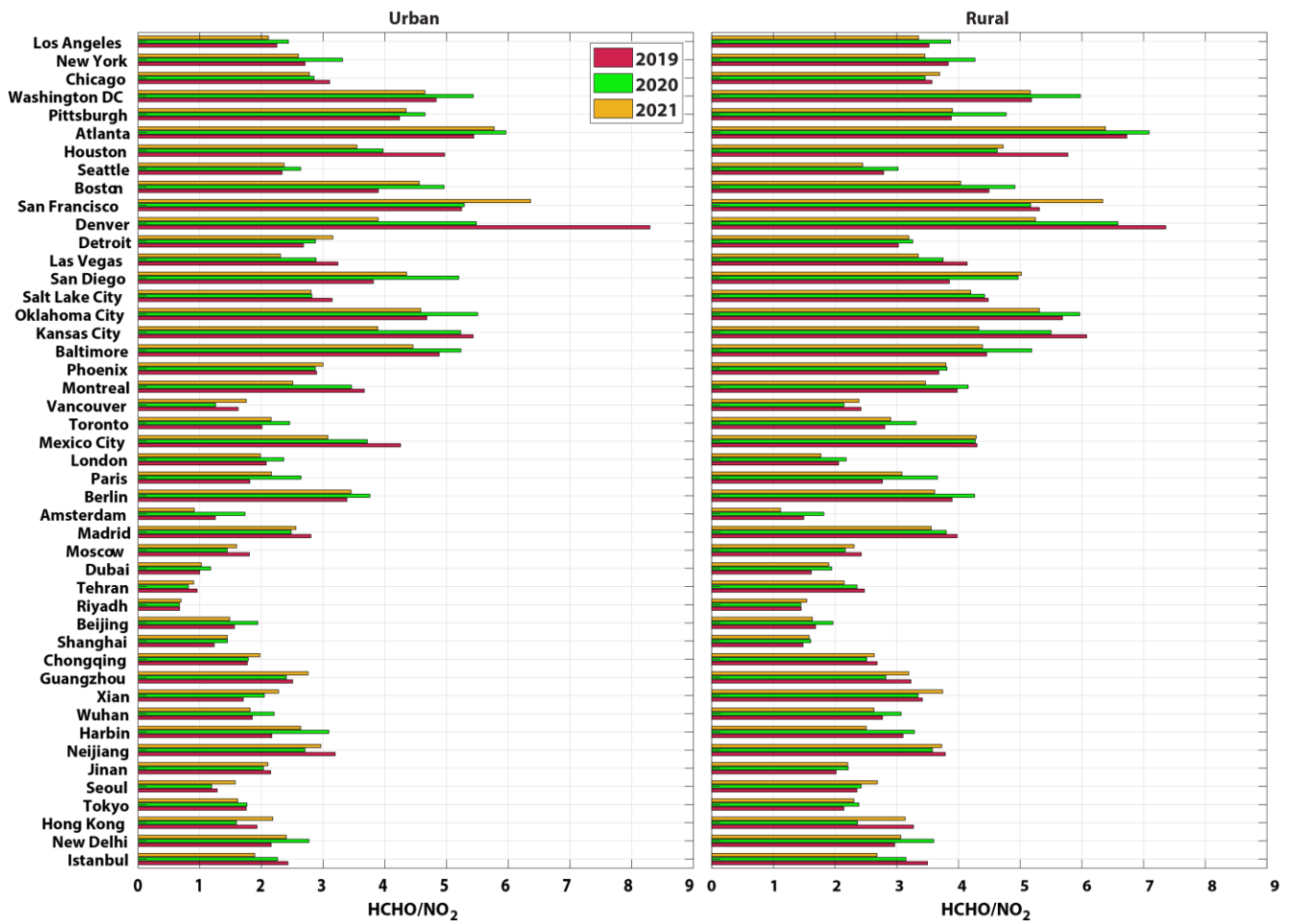
Figure 8: OMI-derived summer-mean (June-August) FNR VCD values for a select 46 cities across the Northern Hemisphere during 2019 (blue), 2020 (red) and 2021 (orange). Each column represents mean FNR values for urban city areas (left column) and the surrounding rural regions (right column).
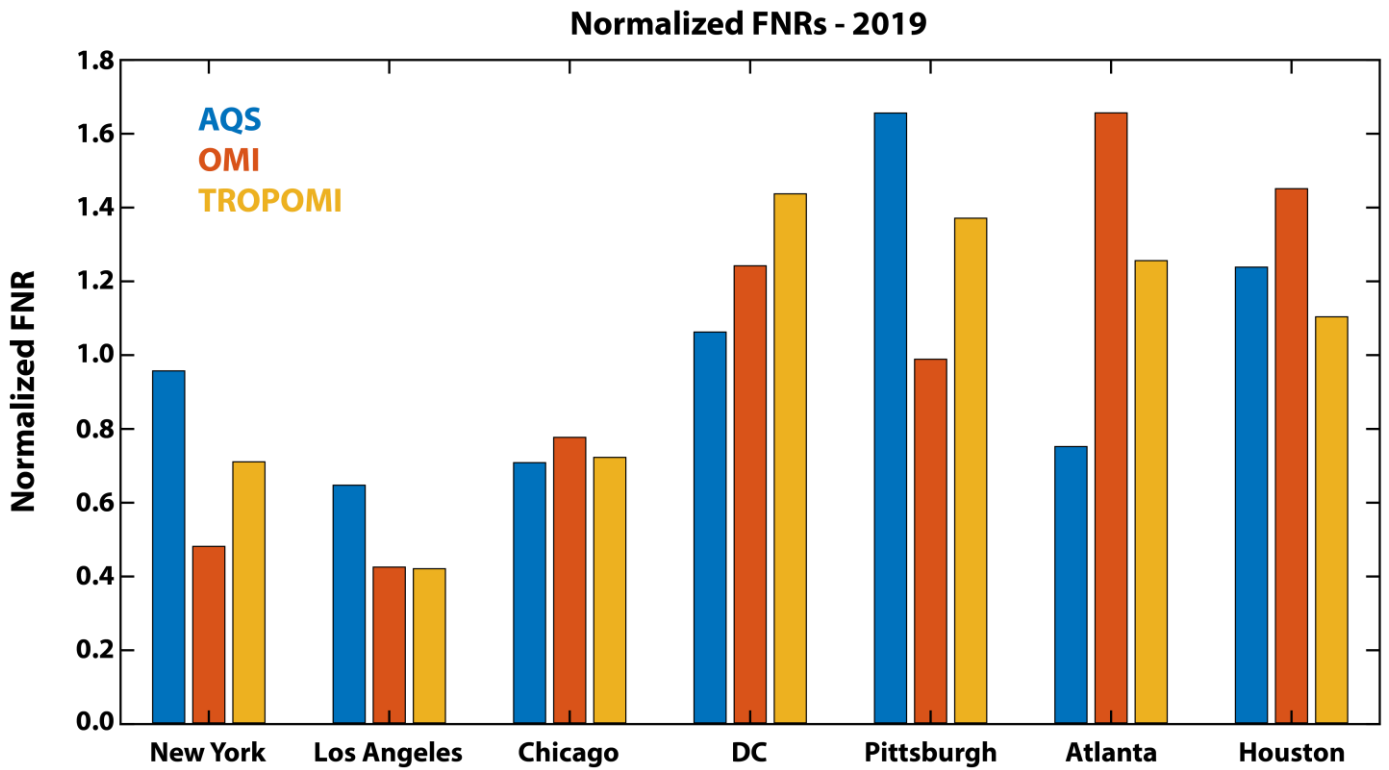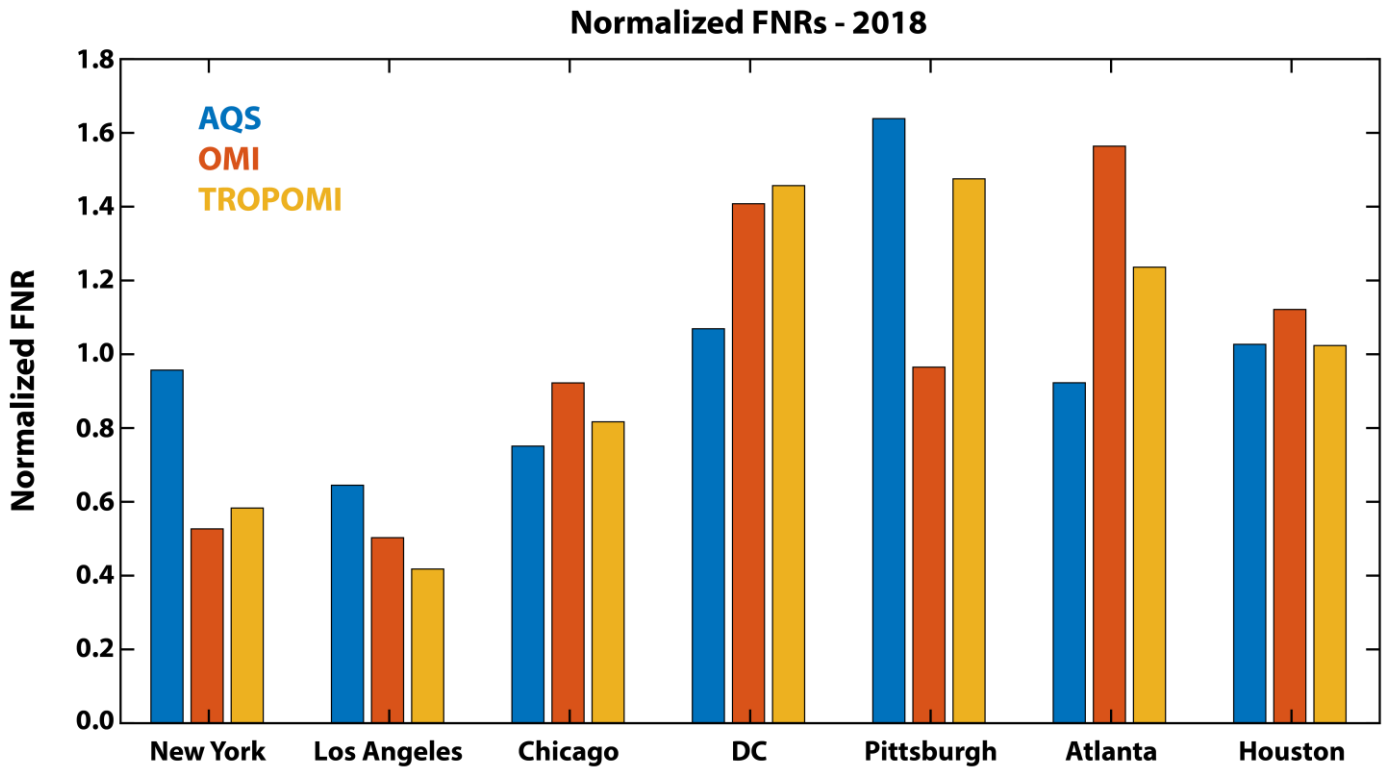
Figure 9: Normalized OMI and TROPOMI summer mean FNRs (each city FNR normalized by the 7-city mean) for each of the 7 selected US cities for 2018 (top) and 2019 (bottom). The same information is shown for surface concentrations from the EPA-AQS in situ observations over the select cities.